



## Controls of local geology and cross-shore/longshore processes on embayed beach shoreline variability

Arthur Robinet, B. Castelle, Déborah Idier, M.D. D Harley, K.D. D Splinter

### ► To cite this version:

Arthur Robinet, B. Castelle, Déborah Idier, M.D. D Harley, K.D. D Splinter. Controls of local geology and cross-shore/longshore processes on embayed beach shoreline variability. *Marine Geology*, 2020, 422, pp.106118. 10.1016/j.margeo.2020.106118 . hal-02506216

**HAL Id: hal-02506216**

**<https://brgm.hal.science/hal-02506216>**

Submitted on 17 Mar 2020

**HAL** is a multi-disciplinary open access archive for the deposit and dissemination of scientific research documents, whether they are published or not. The documents may come from teaching and research institutions in France or abroad, or from public or private research centers.

L'archive ouverte pluridisciplinaire **HAL**, est destinée au dépôt et à la diffusion de documents scientifiques de niveau recherche, publiés ou non, émanant des établissements d'enseignement et de recherche français ou étrangers, des laboratoires publics ou privés.

# Controls of local geology and cross-shore/longshore processes on embayed beach shoreline variability

A. Robinet<sup>a</sup>, B. Castelle<sup>b,c</sup>, D. Idier<sup>a</sup>, M.D. Harley<sup>d</sup>, K.D. Splinter<sup>d</sup>

<sup>a</sup> BRGM, 3 Avenue Claude Guillemin, 45100 Orléans, France

<sup>b</sup> UMR EPOC 5805, Univ. Bordeaux, 33615 Pessac, France

<sup>c</sup> UMR EPOC 5805, CNRS, 33615 Pessac, France

<sup>d</sup> Water Research Laboratory, School of Civil and Environmental Engineering, UNSW Sydney, Manly Vale, NSW, Australia

Corresponding author: A. Robinet, a.robinet@brgm.fr

## Abstract

Shoreline variability along the 3.6-km long Narrabeen Beach embayment in SE Australia is investigated over a 5-year period. We apply the one-line shoreline change model LX-Shore, which couples longshore and cross-shore processes and can handle complex shoreline planforms, non-erodible emerged headlands and submerged rocky features. The model skilfully reproduces the three dominant modes of shoreline variability, which are by decreasing order of variance: cross-shore migration, rotation, and a third mode possibly related to breathing. Model results confirm previous observations that longshore processes primarily contribute to the rotation and third modes on the timescales of months to seasons, while cross-shore processes control the shoreline migration on shorter timescales from hours (storms) to months. Additional simulations simplifying progressively the bathymetry show how the inherent geology strongly modulates the spatial modes of shoreline variability. The offshore central rocky outcrop is found to limit the rotation. In contrast, the submerged rocky platforms that extend from the headlands enhance the shoreline rotation mode and increase alongshore variability of the cross-shore migration mode, owing to increased alongshore variability in wave exposure. Offshore wave transformation across large-scale submerged rocky features and headland shape are therefore critical to contemporary shoreline dynamics.

## Keywords

Embayed beach; shoreline model; local geology; rotation; cross-shore migration; wave transformation

## 1 Introduction

In the context of climate change and increased anthropogenic pressures, it is critical to improve our understanding and predictive capacity of the spatiotemporal evolution of the land-sea interface. Modelling this shoreline variability is challenging given the myriad of driving processes acting at different timescales. Along wave-dominated open and uninterrupted sandy coasts, shoreline variability on the timescales from hours (storm) to years is often primarily driven by cross-shore processes with the shoreline moving rapidly landward (erosion) during storms, and slowly seaward (accretion) during calm periods (e.g. Yates et al., 2009). On longer timescales, other processes such as changes in sediment supply (Thom, 1983) and sea level rise (e.g. Bruun, 1962; Le Cozannet et al., 2016) become important, as well as longshore processes. However, the typical timescales associated with these processes mostly differ on embayed beaches, where inherent geology (rocky headlands, submerged outcrops and rocky platforms extending from the headlands) greatly complicates shoreline response, with longshore processes also impacting shoreline response on short timescales (Ojeda and Guillen, 2008).

Embayed sandy beaches are ubiquitous along hilly or mountainous wave-exposed coasts (Short and Masselink, 1999). The geometry of embayed beaches (headland and beach length) depends on the inherent geology (Fellows et al., 2019), which together with exposure to prevailing wave climate dictate beach morphodynamics (Castelle and Coco, 2012; Daly et al.,

2014) and shoreline change (e.g. Turki et al., 2013). A well-known shoreline behaviour along embayed beaches is clockwise/counterclockwise beach rotation (Klein et al., 2002; Short and Trembanis, 2004; Ranasinghe et al., 2004; Ojeda and Guillen, 2008; Thomas et al., 2010; Loureiro et al., 2013; Turki et al., 2013; Van de Lageweg et al., 2013). While rotation has been observed on the scale of individual storm events (e.g. Harley et al., 2013) and more gradually due to seasonal changes in wave conditions (e.g. Masselink and Pattiaratchi, 2001), it has historically been attributed to longshore sediment transport with the dominant direction of sand movement being associated with the dominant incident wave direction. More recently, Harley et al. (2015) suggested a more complex rotation process whereby alongshore variability in cross-shore sediment fluxes may be more significant at Narrabeen-Collaroy embayment (SE Australia). In addition, other modes of shoreline variability can be observed, such as a so-called 'breathing' mode that represents a change in the overall curvature of the embayed beach (Ratliff and Murray, 2014; Blossier et al., 2017). This mode has been shown theoretically to be driven by longshore processes and to typically explain much less variability of shoreline change than the rotation mode (Ratliff and Murray, 2014).

Over the last decade, a wealth of numerical models has been developed to simulate and further understand shoreline change within coastal embayments. Most of these models are one-line models where shoreline change is essentially driven by longshore processes (e.g. Turki et al., 2013; Ratliff and Murray, 2014). More recently, shoreline change models coupling cross-shore and longshore processes have emerged (Vitousek et al., 2017; Robinet et al., 2018; Antolínez et al., 2019). Amongst these models, LX-Shore (Robinet et al., 2018) can handle complex shoreline geometries (e.g. sand spits, islands), including non-erodible areas such as coastal defences and headlands. New developments to the model also account for non-erodible submerged rocky

structures, providing a unique tool to address the control of geology and cross-shore and longshore processes on shoreline changes in coastal embayments. Although it is well established that both cross-shore and longshore processes combine together to drive shoreline variability along embayed beaches, to our knowledge there is no shoreline modelling study coupling cross-shore and longshore processes and addressing embayed beach dynamics. In addition, most of the modelling studies assume idealized embayed beach bathymetries (e.g. Turki et al., 2013; Ratliff and Murray, 2014). However, it is anticipated that offshore wave transformation over complex bathymetries can have a strong impact on alongshore breaking wave characteristics and, in turn, sediment transport and shoreline response.

The objectives of the present study are two-fold: (1) to identify the respective contributions of cross-shore and longshore processes to the different modes of shoreline variability at a real embayed beach; and (2) to investigate the role of the inherent geology in modulating the spatial and temporal modes of shoreline change. This work relies on the combination of a unique, high-resolution dataset collected at the embayed beach of Narrabeen-Collaroy, SE Australia, and the further application of the LX-Shore one-line shoreline change model. The study site and the LX-Shore model physics are described in detail in Sections 2 and 3, respectively. Model results are then analysed both in terms of spatial and temporal variability in Section 4. Results are discussed in Section 5 before conclusions are drawn in Section 6.

## **2 Study site**

The Narrabeen-Collaroy embayment is a 3.6 km long sandy beach (Turner et al. 2016) located in the northern coastal area of Sydney, Australia (Fig 1a,c), which is hereafter referred to as Narrabeen for conciseness. The sediment is nearly uniform along the embayment and consists of fine to medium quartz sand with a median grain size ( $d_{50}$ ) of approximately 300  $\mu\text{m}$  (Turner

et al. 2016). The beach is bordered by two rocky headlands, which extend offshore through large submerged rocky platforms, with the southern headland being the most prominent (Fig 1c). Just south of the northern headland, an intermittently-active inlet (typically 50 m wide) occasionally connects an inland lagoon to the ocean, which acts more as a sink than a source of sediment to the beach (Morris and Turner, 2010).

The tide at Narrabeen is microtidal and semidiurnal with a mean spring tidal range of 1.3 m (Turner et al. 2016). The beach is exposed to moderate- to high-energy wave conditions with a mean significant wave height ( $H_s$ ) of 1.6 m and a mean peak period ( $T_p$ ) of 10 s. The wave climate is dominated by long period swells coming from the SSE (Fig 1.b), generated by eastward-tracking extratropical cyclones south of mainland Australia. The coast is also exposed to storm waves from the S, E and NE generated by intensified extratropical cyclones, east coast lows, and tropical cyclones, respectively. The wave climate is slightly seasonally-modulated owing to decreasing extratropical cyclone and east coast low activity in the austral summer along with more NE sea breezes generating short-period waves. The wave climate offshore of Narrabeen is termed storm-dominated as energetic wave conditions occur all year long (Splinter et al., 2014).

Nearshore wave conditions at Narrabeen are non-uniform alongshore due to refraction, bottom friction and depth-induced breaking enforced by the complex inherent geology (Fig. 1c). The south headland shelters the southern part of the beach from waves coming from the S-SE (Bracs et al., 2016), leading to up to 30% difference in breaking wave height from S to N for average conditions (Harley et al., 2011a). Within the embayment, the bottom is essentially sandy from the subaerial beach to at least 20-m depth. Exceptions to this sandy bed are made in front of the northern and southern end of the beach, where small rocky outcrops lying in

depths from 5 to 10 m disturb the relatively shore-parallel bathymetric iso-contours. Apart from relatively small rocky areas, a large rocky outcrop is observed approximately 1 km offshore in the centre of the embayment, with a minimum depth at its crest of approximately 18 m (Fig 1b). Previous wave modelling suggests that, during energetic storm events, this geological feature affects wave propagation through a combination of refraction, diffraction and bottom friction (Bracs et al., 2016).

The beach state is modally intermediate-dissipative in the north and progressively transforms into intermediate-reflective towards the S. The subaerial beach width can vary by up to 80 m (70 m) in the north (south). The beach is backed by high natural and vegetated foredunes in the north, while in the central and southern part of the beach intensive urbanization has led to the replacement of natural dunes by sea-facing properties typically protected by buried rubble mound sea-walls.

A continuous beach survey program has been led since 1976 at Narrabeen, creating one of the most extensive shoreline datasets worldwide (Turner et al., 2016). Among the numerous cross-shore transects initially defined to support this program, five (PF1, PF2, PF4, PF4 and PF8) have been continuously used to conduct biweekly beach profiles (transects are shown in Fig. 1b). Since 2005, this survey program has included monthly three-dimensional topographic surveys of the entire 3.6 km-long subaerial beach using an all-terrain vehicle (Harley et al., 2011b). Previously, Harley et al. (2015) performed an empirical orthogonal function (EOF) analysis on a 5-year period (2005-2010) of this three-dimensional dataset and showed that the two dominant modes of shoreline variability are cross-shore migration followed by rotation, explaining approximately 55% and 22% of the overall variability, respectively. A third mode of variability explaining less than 10% of the total variance was disregarded in their analysis.

Below we address the same period as that investigated in Harley et al. (2015), but focussing on shoreline variability from both measurements and model outputs.

### **3 LX-Shore application**

#### **3.1 Model description**

LX-Shore is a two-dimensional planview cellular-based one-line shoreline change model for wave dominated sandy coasts (Robinet et al., 2018). An overview of the model is provided in Fig. 2 and the reader is referred to Robinet et al. (2018) for more details. LX-Shore simulates shoreline change resulting from the combination of gradients in total longshore sediment transport and cross-shore transport driven by changes in incident wave energy (Fig 2a,c). LX-Shore can handle complex shoreline geometries (e.g. sand spits, islands), including non-erodible areas such as coastal defences and headlands.

Unlike usual one-line models directly resolving the shoreline position (e.g. Hanson, 1989; Kaergaard and Fredsoe, 2013; Hurst et al., 2015; Vitousek et al., 2017), and in line with Ashton and Murray (2006), LX-Shore computes changes in the relative amount of dry (i.e. land) surface in square cells discretizing horizontally the computation domain and presenting a typical spatial resolution of 10-100 m (Fig. 2b). This relative amount, hereafter referred to as the sediment fraction, ranges from 0 (water cells) to 1 (fully dry cells). The planview shoreline is then retrieved at each simulation timestep using an interface reconstruction method. Change in sediment fraction within the cells can result from longshore transport computed using the formula of Kamphuis et al. (1991), which can be multiplied by a free calibration parameter ( $f_{ql}$ ) when data is available for calibration. Sediment fraction changes also result from cross-shore transport using an adaptation of the equilibrium-based ShoreFor model (Davidson et al., 2013;



Splinter et al., 2014). Here the disequilibrium term is computed from offshore wave conditions instead of breaking wave conditions. This cross-shore module is based on three model free calibration parameters (for more detail the reader is referred to Davidson et al., 2013; Splinter et al., 2014): the response factor  $\Phi$  that describes the ‘memory’ of the beach to antecedent wave conditions; the rate parameter  $c$  that describes the speed at which the shoreline erodes/recovers; and a linear trend parameter  $b$ .

LX-Shore incorporates the direct formula of Larson et al. (2010) to rapidly compute the wave characteristics at breaking at each time step, which is typically used on simple and academic application cases (Robinet et al., 2018). Here the coupling with the spectral wave model SWAN (Booij et al., 1999) is used to account for the complex wave transformation at Narrabeen. LX-Shore, in turn, provides at each time step an updated bathymetry that feeds back onto wave transformation. This updated bathymetry is reconstructed (Fig. 2a) using a method similar to the one used by Kaergaard and Fredsoe (2013), from the current shoreline position and an idealized static equilibrium beach profile (a Dean profile).

For the present study, the bathymetric reconstruction method presented in Robinet et al. (2018) has been improved by allowing real non-erodible bathymetric features to be included in water depths greater than a threshold depth ( $D_t$ ). Beyond this depth, the idealized bathymetry is replaced by the measured bathymetry.  $D_t$  must be greater than the depth of closure ( $D_c$ ) to maintain the equilibrium beach profile which is a fundamental assumption of the one-line modelling approach. Note that a merging is applied over a buffer area between  $D_c$  and  $D_t$  to ensure a smooth transition between idealized and measured bathymetries. This improvement allows testing the effect of complex local geology such as that observed at Narrabeen on the different modes of shoreline variability.

## 3.2 Data

### 3.2.1 Waves and wind

LX-Shore simulations are conducted using offshore wave conditions ( $H_s$ ,  $T_p$  and peak wave direction  $D_p$ ) measured by the Sydney buoy located 11 km to the southeast of Narrabeen in approximately 80-m depth. Similar to Harley et al. (2015), gaps in buoy measurements were filled using wave conditions extracted from the CAWCR hindcast (Durrant et al., 2014). Inshore wave conditions measured by a waverider buoy deployed at the centre of the embayment in 10-m depth from July 21 to November 14, 2011 were also used to validate the modelled wave conditions close to breaking. As justified in section 3.4, SWAN was also forced by the wind conditions measured at Sydney airport.

### 3.2.2 Bathymetry and seabed type

Three different bathymetric data sources were used to generate the bathymetries associated with the SWAN computation grids introduced in Section 3.3.3. The first, most-inshore, bathymetry was sourced from sixteen surveys conducted using a single-beam echosounder mounted to a jetski within the Narrabeen embayment between April 2011 and May 2017. These sixteen bathymetries were averaged to obtain a representative bathymetry of the embayment. Remaining gaps in the bathymetry over the LX-Shore simulation domain were subsequently filled using a second bathymetric dataset of 2-m-spaced iso-bathymetric contours covering the Sydney coastal waters down to 50 m depth digitised from bathymetric charts by the NSW Office of Environment and Heritage (NSW OEH). For even deeper waters, the large-scale coarse-resolution Australian Bathymetry and Topographic Grid (ABTG, Whiteway, 2009) was used. Rocky seabed contours were extracted from the mapping of subtidal habitats provided

by the NSW OEH and used to identify the non-erodible rocky patches within and outside the embayment.

### **3.2.3 Shoreline and rocky contours**

Contours of the northern and southern Narrabeen headlands were digitalized manually from Google Earth. For LX-Shore calibration and validation, 44 complete planview shorelines derived from the all-terrain vehicle topographic surveys conducted from July 2006 to July 2010 with an average periodicity of 30 days were used (Harley et al., 2015). Following Harley et al. (2015), the mean-sea-level contour was used as the shoreline proxy throughout. The beach topographic survey conducted on July 22, 2005 was also used to compute the initial shoreline position in our simulations as detailed in Sections 3.3.1 and 3.3.2.

## **3.3 Setup**

### **3.3.1 General settings**

The model is applied over a 5-year period from July 2005 to July 2010, which is the period studied in the reference work of Harley et al. (2015). The simulation timestep is set to 3 hours for both LX-Shore and SWAN. The equilibrium beach profile used in LX-Shore was calibrated using the time and spatial average of the beach profiles measured along transects PF2, PF4 and PF6 (Fig. 1b) down to nearly 14-m depth. PF1 and PF8 were excluded due to the prominence of rocky outcrops at these locations. The depth of closure used in LX-Shore simulations was obtained from the following steps: (i) offshore wave conditions from July 2005 to July 2010 were propagated shoreward using SWAN, based on the computation grids and model settings described in Sections 3.3.3 and 3.4, respectively; (ii) wave conditions were extracted in 10-m depth offshore the five historical transects and then used to estimate a few theoretical values of  $D_c$  along the beach, based on the formula of Hallermeier (1981); (iii) because estimates of  $D_c$

ranged from 6.2 to 8 m, a near average value of 7 m was taken as representative of  $D_c$  for the entire embayment. The implications related to the choice of this depth of closure are discussed later in Section 5.2.

### **3.3.2 Initial conditions**

The rocky contours are considered non-erodible and remain unchanged during the model simulations. The initial shoreline condition is the planview shoreline measured by the all-terrain vehicle on July 22, 2005. However, preliminary tests showed that the mean shoreline planform simulated with LX-Shore tends to slowly converge towards a slightly different shape than that observed, which is a common problem in shoreline change modelling (e.g. Antolínez et al., 2019). Given that the objective of the present study is to investigate the spatial and temporal shoreline variability and not the mean shoreline planform, the deviation from the respective mean of the modelled and measured shoreline was compared. To avoid bias induced by model spin-up from the initial measured shoreline position, a two-step simulation workflow was designed (see Fig. 3). First, a spin-up simulation was run from the initial measured shoreline position to obtain a quasi-converged planview shoreline by averaging the planview shoreline simulated during the last year of the simulation period. Then, this quasi-converged planview shoreline was used as input to a new simulation over the same period. Because the first year of this second simulation still involves some model spin-up, it is removed from further analyses, therefore the results presented here concentrate only on the 4-year period from July 2006 to July 2010.

### **3.3.3 Computation grids and role of inherent geology**

A modelling strategy using a nested SWAN computation grid was adopted to speed up the simulations (Fig. 4a). The coarser hydrodynamic grid is regular with a mesh resolution of 50 m

and is based on a bathymetry computed by merging the 2 m iso-contour bathymetry with the deeper ABTG bathymetry (Fig. 4a). Depths from the 2 m iso-contour dataset are kept from 0 to nearly 40 m depth and are then progressively merged with the coarser ABTG bathymetry data down to nearly 50 m depth, below which only ABTG data are used.

The nested refined hydrodynamic grid is regular, with a 20-m mesh, and is based on the bathymetry produced iteratively by LX-Shore as described in Section 3.1. The measured bathymetry used in the merging process is made of the combination of the time-averaged jetski-based bathymetries and the 2 m iso-contour dataset. Fig. 4b shows an example of the merged bathymetry produced by LX-Shore. The morphological grid used in LX-Shore (Fig. 4c) has the same spatial extent as the refined hydrodynamic grid but with a cell width of 80 m. The shoreline is discretized into nearly 40 cells. To explicitly test the influence of the inherent local geology on the different modes of shoreline variability at this embayed beach, additional simulations were performed using alternative bathymetries for the refined grid. The central rocky outcrop was removed from the nearshore bathymetry (Fig. 5b) and the bathymetry was also further idealized by removing submerged rocky platform headland extensions and replacing it with a Dean profile along the entire embayment (Fig. 5c), showing large seabed elevation differences (Fig. 5d).

### **3.4 Calibration**

Prior to LX-Shore simulations, a preliminary task consisted of calibrating SWAN parameters to improve wave hindcasts within the embayment. Calibration was made using inshore wave conditions measured at the centre of the embayment in 10-m depth (Fig. 4a,b white triangle) from July 21 to November 14, 2011 (no other observations were available during the simulation period). The default directional spreading of 30° was increased to 45°. The friction was enabled

using the expression of Madsen et al. (1988) and a non-uniform bottom roughness length scale. The default value of 0.05 m was used for sandy seabed, but this value was set to 0.5 m for rocky seabed. Finally, the wave generation by wind and dissipation through whitecapping were enabled using the expressions of Komen et al. (1984). Modelled  $H_s$  and mean wave direction ( $D_m$ ) show good skill (Table 1) with a root mean squared error (RMSE) of 0.17 m and  $10.13^\circ$  and with a correlation coefficient of 0.94 and 0.75, respectively. Modelled mean wave period ( $T_m$ ) is less accurate with a RMSE of 1.54 s and a correlation coefficient of 0.60. The present, more-refined, model setup reduces the bias in  $D_m$  from  $4^\circ$  to  $0.71^\circ$  in comparison with the reference look-up table used to predict inshore waves at Narrabeen in Turner et al. (2016). The cross-shore model was calibrated by optimizing three free model parameters. Here, a simulated annealing optimization algorithm (Bertsimas et al., 1993) was used as in Castelle et al. (2014) to find the optimal coefficient combination to simulate the cross-shore shoreline positions measured at PF6. The optimized values for these coefficients are as follows:  $\Phi = 35$  days;  $c = 2.5304 \times 10^{-7} \text{ m}^{1.5} \text{ s}^{-1} \text{ W}^{-0.5}$ ;  $b = 1.4695 \times 10^{-7} \text{ ms}^{-1}$  and were further used for the entire embayment. For the longshore transport model, simulations were conducted by increasing  $f_{Ql}$  to 3, 4 and 5. A fair comparison regarding the changes of the overall shoreline orientation (defined as the angle between the north and the linear fit of the northward shoreline positions) was achieved for  $f_{Ql} = 4$ .

### 3.5 Post-processing of shoreline position

To ease the analysis of measured and simulated shoreline change, the Cartesian coordinates ( $x, y$ ) of shoreline positions were transformed into alongshore – cross-shore ( $s, p$ ) coordinates following the method introduced by Harley and Turner (2008). This transformation relies on a logarithmic spiral baseline obtained by fitting a reference planview shoreline. Here, the

average planview shoreline over the study period without model spin-up (July 2006 – July 2010) is used as the reference, with  $p$  indicating the cross-shore distance from the time-averaged cross-shore shoreline position and  $s$  indicating the alongshore distance from the northern end of the beach. Because of the slight differences between the measured and modelled time-averaged shoreline planforms, two distinct logarithmic spirals were used as reference planforms to analyse shoreline variability (one for the model, one for the observations). These two distinct reference planforms were used to more accurately define the longshore and cross-shore directions in the measured and modelled datasets.

## **4 Results**

### **4.1 Simulated shoreline changes**

Fig. 6a shows the observed and simulated time-averaged planview shorelines. Although the overall shape is fairly well captured by the LX-Shore model, substantial changes of up to 30-40 m cross-shore can be observed (Fig. 6b). The planform curvature is underestimated by the model, resulting in a mean modelled shoreline position located further offshore in the centre of the embayment and further inshore close to its extremities. Although accurately simulating the mean shoreline planform of the coastal embayment is not an objective of the present study, this limitation will be discussed later in the paper (refer Section 5). Hereafter, the cross-shore deviation of observed and modelled shoreline from their respective means  $p(s,t)$  is addressed.

Fig. 7 shows the space-time diagrams of the modelled (Fig. 7b,c) and measured (Fig. 7d) shoreline deviation from the mean with corresponding time series of the five historical profiles (PF1, PF2, PF4, PF6 and PF8) shown in Fig. 8. A number of erosion events along the entire embayment can be seen. The June 2007 event stands out (Fig. 7b-d), which was caused by an

intense east coast low in the northern Tasman Sea on 7-10 June driving high-energy waves from the SE reaching 6.9 m offshore (Fig. 7a), and resulting in 273,000 m<sup>3</sup> of sand removed from the subaerial beach (Harley et al., 2015). The shoreline retreat due to this event was observed to be on the order of 30-40 m at all five profiles, except at the southern profile PF8 where erosion reduced to approximately 20 m (Fig. 8). Rapid erosion events were followed by slower recovery periods typically extending a few months (Fig. 7d). Overall, shoreline varied more at the north of the embayment than at the south, owing to the larger exposure to the prevailing wave conditions from the SE (Harley et al., 2015). A number of clockwise and counter-clockwise rotation events can be observed (Fig. 7d), which are sometimes not associated with an overall migration of the shoreline.

Similar shoreline change patterns are observed with the model (Fig. 7c), which can provide much higher frequency insight into erosion and rotation signals using output at each model time step (Fig. 7b). The model readily captures erosion and subsequent multi-month recovery of the shoreline, as well as rotation events (Fig. 7c-e). Given that the model does not explicitly include surfzone sandbar dynamics, the model does not capture the short-scale, alongshore shoreline variability (e.g. around May 2009), which may reflect the presence of megacusp embayments observed previously at this site (e.g. Harley et al., 2015; Splinter et al., 2018). Fig. 7b also shows that shoreline recovery is not a steady process, instead, significant interruptions and reversals in recovery are caused by more or less small storm events. This is further emphasized in Fig. 8. The model systematically explains more than 70% of shoreline variance at all transects (Fig. 8) except at the southern profile FP8 (42%, Fig. 8e), with root mean squared errors systematically smaller than 7.5 m (Fig. 8). Importantly, the model is also able to capture



extreme accretion-erosion events, which were typically underestimated north of the beach in previous modelling efforts (e.g. Splinter et al., 2014).

## **4.2 Temporal and spatial modes of shoreline variability: LX-Shore capabilities**

To better understand the different modes of shoreline variability within the embayment, an EOF analysis was performed to decompose observed shoreline variability into linear combinations of statistically independent spatial and temporal patterns (Miller and Dean, 2007). Results of the first three EOFs from measured cross-shore shoreline deviation from the mean  $p(s,t)$  (Fig. 7d) are presented in Fig. 9. These results indicate very similar modes of shoreline variability to those obtained in Harley et al. (2015). This is in spite of the fact that the former study includes an additional one year of shoreline data that is disregarded here due to model spin-up. The primary modes of shoreline variability are, by decreasing order of importance: (i) cross-shore migration with larger amplitude in the north and accounting for 61.3% of the variance; (ii) beach rotation accounting for 19.2% of the variance and presenting a nodal point near  $s = 1800$  m and an attenuation of the spatial mode at  $s = 800$  m; (iii) a third mode accounting for 6.2% of the variance.

A similar analysis was performed with model outputs at time steps concurrent with measurements (Fig. 7c). Results (Fig. 9, red lines/dots) show that the EOF analysis gives, in the same order of importance, very similar spatial patterns (Fig. 9a-c), although the model gives more variance (81.6%) to the first mode (cross-shore migration) than measurements (61.3%). It is however important to note that the model was not calibrated on these modes of variability, and that slight changes in the free parameters could lead to better agreement, which will be discussed later in the paper (refer Section 5). The corresponding modelled temporal modes of

variability are also in very good agreement with measurements, particularly for the two first modes ( $R^2 > 0.8$ ) and to a lesser extent the third one ( $R^2 = 0.68$ , Fig. 9d-f).

#### **4.3 Respective contribution of longshore and cross-shore processes to shoreline variability on the timescales from storm to years**

Because modelled temporal and spatial modes of shoreline variability are in very good agreement with observations, LX-Shore can be used to further address the respective contributions of cross-shore and longshore processes to the different modes of shoreline variability. For this purpose, cross-shore or longshore processes were switched off alternatively and the impacts on the modes of shoreline variability were investigated systematically. Using model outputs at each model time step (3 hours) instead of only at the time steps concurrent with measurements (~monthly), also provides insight into the shoreline response timescales. The three top panels in Fig. 10 show the first three EOFs with both cross-shore and longshore processes included. Spatial modes (cross-shore migration, rotation and the third mode) are essentially similar in pattern (Fig. 9a,b,c), with the high-frequency temporal modes showing a large number of reversals and short-term large changes highlighting the dynamic nature of the embayment. Visual inspection of Fig. 10h,i,j (comparison of blue lines) also reveals different temporal dynamics for the three modes of variability. While the cross-shore migration mode occurs on scales of hours (storm) to months (Fig. 10h), the rotation mode operates more gradually on annual and interannual scales (Fig. 10i). This is in line with Harley et al. (2015) who showed that the first EOF was controlled by waves averaged over ~ 8 days (representing storms) whereas the second EOF was more controlled by wave changes over months to seasons. Regarding the third mode, no

predominant timescale arises as both short-term (event scale) and long-term (annual scale) temporal patterns superimpose.

Running LX-Shore with cross-shore processes switched off (i.e. longshore only), the EOF analysis shows that the primary modes of shoreline variability in such a configuration (Fig. 10d,e) are essentially similar in pattern to the second (rotation) and third modes (Fig. 10b,c). The corresponding temporal modes (Fig. 10k,l) are also essentially the same as for the simulation combining cross-shore and longshore processes (Fig. 10i,j). Running LX-Shore with longshore processes switched off (i.e. cross-shore only), the EOF decomposition leads to two dominant modes of shoreline variability (Fig. 10f,g,m,n). The first mode corresponds to a short-term cross-shore shoreline migration, which is maximized along the northern part of the beach and decreases to close to 0 towards the south (Fig. 10f,m). The negative trend in the temporal EOF, combined with the shape of the spatial EOF, indicates that during the simulation this first mode tends to drive a long-term shoreline retreat, which increases northwards. In contrast, the second mode corresponds to a beach rotation with an amplitude maximized along the southern part of the beach (Fig. 10g,n). The positive trend in the temporal EOF, combined with the shape of the spatial EOF, indicates that during the simulation this second mode tends to drive a long-term shoreline retreat and advance at north and south, respectively. Given that the temporal EOFs of these two modes are similar, and that the first mode shows more variance, the combination of these two modes mostly corresponds to the cross-shore migration mode of the LX-Shore simulation accounting for both cross-shore and longshore processes. In brief, LX-Shore simulations indicate that longshore processes primarily contribute to the second (rotation) and third modes of shoreline variability (Fig. 10b,c), while cross-shore processes control the cross-shore migration with more variability at

the northern end (Fig. 10a). These results corroborate those of Harley et al. (2011a, 2015) based on extensive field data analysis, showing that LX-Shore can be a powerful tool to address the modes of shoreline variability in complex settings.

#### **4.4 Controls of inherent local geology on the shoreline modes of variability**

As shown in Fig. 1b, Narrabeen is bordered by two prominent and morphologically different rocky headlands, which extend offshore through large submerged rocky platforms. In addition, a large rocky outcrop located approximately 1.5 km offshore in less than 20-m depth can be observed. This inherent local geology can affect wave propagation, breaking wave conditions along the embayment and, in turn, the modes of shoreline variability. To further test this hypothesis, two additional simulations (including wave and shoreline modelling) were performed using the same free parameters as in the reference simulation: one removing the prominent central rocky outcrop (Fig. 5b) and a second simulation further removing the headland-facing submerged rocky platforms (including the central rocky outcrop) through a Dean profile along the entire embayment (Fig. 5c).

Results from EOF decomposition applied to the outputs of these two additional simulations are superimposed in Fig. 11 onto those from the reference simulation. It appears that removing the central rocky outcrop only slightly affects the overall modes of shoreline variability (Fig. 11, red lines). This suggests that the outcrop is too deep to enforce strong wave energy focusing that would cause alongshore gradients in breaking wave conditions large enough to modify both modal wave exposure and longshore sediment transport patterns. This is illustrated in Fig. 12 that shows that even for representative prevailing high-energy waves from the SSE, the wave height patterns alongshore (Fig. 12b) are very similar to those simulated with the reference bathymetry (Fig. 12b,d,e). Two substantial effects can however be highlighted. First,

434 the spatial pattern of the second (rotation) mode is more uniform alongshore (Fig. 11b),  
435 suggesting that the presence of this relatively deep central rocky outcrop increases shoreline  
436 response complexity. Second, the importance of the rotation mode increases by approximately  
437 46% (from 10.9% to 15.9% of the total variance, Fig. 11b) when removing the outcrop,  
438 suggesting that the central rocky outcrop is a limiting factor to the rotation signal of the  
439 embayment. The simulation for which the bathymetry is further idealized (i.e., with the  
440 submerged rocky platforms at the two extremities also removed, refer Fig. 5c) shows much  
441 larger changes on shoreline variability (Fig. 11, green lines). The first (cross-shore migration)  
442 mode is more uniform along the embayment (Fig. 11a). This observation is consistent with  
443 Harley et al. (2015), who suggest that the asymmetric spatial EOF of the cross-shore migration  
444 mode is related to alongshore variability in wave exposure, which is indeed reduced when  
445 idealizing the offshore bathymetry (see wave field for a SSE swell in Fig. 12c). Overall, the  
446 spatial patterns of the second (rotation) and third modes are also more uniform along the  
447 embayment without the complex submerged rocky platforms. In addition, the contribution of  
448 the second (rotation) mode is reduced by 36% with respect to simulations where only the  
449 central rocky outcrop is removed (from 15.9% to 10.1%). This suggests that the prominent  
450 submerged rocky platform extensions from the headlands enhances the shoreline rotation  
451 mode at Narrabeen. Wave refraction around the prominent platforms resulting in more  
452 alongshore non-uniform breaking wave conditions and, in turn, stronger longshore sediment  
453 transport gradients, is therefore hypothesized to increase the degree of shoreline rotation.

## 5 Discussion

### 5.1 Respective contributions of inherent geology and cross-shore and longshore processes

For the first time our simulations allowed isolating the respective influence of the inherent geology and the cross-shore and longshore processes on the dominant spatial and temporal modes of shoreline variability at a real embayed beach. Although our findings cannot be generalized to all coastal embayments, they provide new insight into shoreline dynamics on real embayed beaches. Overall our results show that longshore processes primarily contribute to the second (rotation) and third modes of shoreline variability at this site, while cross-shore processes control the alongshore-averaged, cross-shore migration, with the inherent geology modulating the modes in space. An important result is that the inherent geology can have a significant impact on shoreline dynamics from the timescales of storms to years. Inherent geology has long been known to influence beach states (Jackson et al., 2005), rip channel morphodynamics (Castelle and Coco, 2012; Daly et al., 2014) or extreme erosion (Loureiro et al., 2012). Here we demonstrate that not only does the headland geometry have an impact on shoreline change, but also more localised submerged rocky outcrops both at the centre and extremities of the embayment. The influence of such submerged non-erodible morphology has been disregarded in previous shoreline change studies, except in a few studies such as Limber et al. (2017) who only investigated the time-averaged shoreline position. These results have implications from the perspective of coastal engineering. Hard structures such as groynes (Hanson et al., 2002) or submerged breakwaters (Bouvier et al., 2017, 2019) are often designed based on their impacts on the adjacent mean shoreline position. Here we show that the design of such structures should also consider their impact on the modes of shoreline variability,

including beach rotation and other higher-order modes. These can indeed drive localized time-limited severe erosion on artificial embayed beaches (Ojeda and Guillen, 2008).

The third mode of shoreline variability, which is reasonably reproduced by the model (Fig. 9c), was suggested by Harley et al. (2015) to potentially be driven by ebb inlet processes occurring at the northern extremity of the beach. The inlet, however, is not included in LX-Shore, which suggests that the influence of the inlet on the shoreline variability is relatively minor and that this third mode is related to other processes. An alternative control of this third mode of shoreline variability is the localized rocky outcrop located in 5 to 10 m depths towards the northern extremity of the beach at around  $s = 150$  m. Indeed, when present in the bathymetry, this rocky outcrop is observed to cause substantial localized focusing of breaker wave energy (Fig. 12a,b,d,  $s = 150$  m). With this rocky outcrop smoothed within an idealized bathymetry, relatively uniform longshore breaker wave heights are observed (Fig. 12c,d,  $s = 150$  m), resulting in weakly spatially varying longshore transport. In contrast, such inherent geology, which results in stronger alongshore variability in breaking wave characteristics and, in turn, longshore transport, is likely to drive more complex shoreline variability in its lee. The shape of the spatial EOF of the third mode becomes more symmetrical when idealizing the bathymetry (Fig. 11c) and resembles the U-shaped breathing pattern identified in Ratliff and Murray (2014). The translation of the U-shaped patterns towards the north for the idealized bathymetry might be related to offshore waves predominantly coming from the SE at Narrabeen (Fig. 1b,c,d), whereas in Ratliff and Murray (2014) only symmetrical distributions of wave direction centred around the beach normal are used to force shoreline changes. At this stage it is however not possible to refer to this third mode as “breathing”, which only represents 6.2% of the observed shoreline variability during the period studied here.

Both measurements and model results indicate that the cross-shore migration mode is dominant, followed by the rotation mode during the period studied here. However, it is well established that the wave climate at Narrabeen shows strong interannual variability (Ranasinghe et al., 2004; Harley et al., 2010) and that changes in seasonality of storms can have a profound impact on shoreline behaviour (Splinter et al., 2017; Dodet et al., 2019). It is therefore anticipated that the respective contributions of the different modes of shoreline variability to the total shoreline variance may change over time. It will be important to address shoreline variability on longer timescales and explore the genericity of our findings at Narrabeen.

## **5.2 LX-Shore limitations and opportunities**

Our approach presents a number of limitations which are discussed below. First, it is important to remind the reader that, even if LX-Shore relies on an accurate modelling of the waves, it falls into the hybrid shoreline model category, i.e. models based on general principles (e.g. behavioural laws, semi-empirical rules). These models do not use detailed hydrodynamics (nearshore circulation), sediment transport and mass conservation equations. Therefore, while these models can be applied over larger temporal and spatial scales with reasonable computation cost, they also rely on basic assumptions (see Robinet et al., 2018 for detailed assumptions of LX-Shore). Because of this, hybrid models can only be used to investigate the embayed beach mechanisms driven by the processes resolved and at scales at which these processes are meaningful. In contrast, physical-based morphodynamic models have the theoretical potential to explore the full range of mechanisms involved in embayed beach development and dynamics (e.g. Daly et al., 2014, 2015), although they require long and possibly discouraging computation time (Daly et al., 2014). The LX-Shore component



resolving longshore processes uses an empirical formula to compute alongshore sediment transport and ensures mass conservation. In contrast, the cross-shore-processes are resolved using an approach relying on a time-varying wave-based equilibrium that does not consider mass conservation. In brief, LX-Shore assumes that the beach cross-shore profile remains unchanged and only translates as the cross-shore shoreline position evolves. This means that deposition or erosion of sediment uniformly spreads along the entire profile from the depth of closure to the top of the active profile. This profile is assumed uniform alongshore, whereas at Narrabeen the mean beach profile characteristics substantially vary alongshore, as does the depth of closure, owing to increasing exposure northwards to the prevailing waves coming from the SE (Harley et al, 2011a). This assumption likely explains a part of the model-data disagreement, in particular the difference in time-averaged shoreline planform in Fig. 6. This depth of closure concept is also challenged along embayed beaches where sediment bypassing (McCarroll et al., 2019; Valiente et al., 2019) and headland rips flushing the surf zone (Castelle and Coco, 2013) have the potential to transport sediment into a nearby embayment and/or well beyond the depth of closure. All these embayed beach specific processes are not taken into account in the present version of LX-Shore.

The choice of the depth of closure is crucial in reduced-complexity shoreline change modelling based on the one-line approach (Robinet et al., 2018) as the magnitude of the shoreline response to gradients in alongshore sediment transport depends on this parameter (inverse relation of proportionality). It may also modulate the relative contribution of alongshore processes to shoreline changes in case additional  $D_c$ -independent drivers of shoreline variability are included (e.g. cross-shore processes included in LX-Shore). It is therefore essential to use a  $D_c$  value that matches the timescales considered and the processes

investigated. In LX-shore, the cross-shore processes are resolved on the timescales from storms up to years. The short period used to compute  $D_c$  (5 years) ensures a match between the timescales associated with the cross-shore and longshore processes and allows comparing their respective contribution. Addressing long timescales at Narrabeen with LX-Shore (e.g. decades) should imply a re-evaluation of  $D_c$  (increased value), which may lead to underestimate on short timescales (storms to years) the shoreline response to alongshore processes relatively to that driven by cross-shore processes. At sites where the number of bathymetric surveys is insufficient,  $D_c$  can still be computed from wave-based formulas (e.g. Hallermeier, 1981; Ortiz and Ashton, 2016) or extracted from a new global database of  $D_c$  (Athanasίου et al., 2019). The theoretical framework proposed by Ortiz and Ashton (2016), which relies on local wave conditions and few physical parameters, provides an objective method to determine  $D_c$  according to the timescales of interest. Based on the average wave conditions simulated along the 10-m depth contour and considering a 5-yr-timescale, their approach gives a  $D_c$  ranging from 7.2 to 8.8 m. Given the similarity between these values and those obtained with the formula of Hallermeier (1981) and given the apparent match between measured and simulated modes of shoreline variability (Fig. 9), a  $D_c$  of 7 m seems appropriate for the range of timescales involved in this study (storms to years).

We performed model calibration on the shoreline position along a single transect and on the change in planview shoreline orientation (linear fit) for the cross-shore and longshore model components, respectively. It was chosen to mimic the classic calibration method, i.e. minimizing the error between simulated and measured values of the latter variables. However, calibrating the model on the amount of variance of the three dominant modes of shoreline variability would likely have further improved model-data agreement. In other

words, we willingly decided not to calibrate the model on the end product. Optimization of the cross-shore model free parameters was made at transect PF6 ( $s \approx 2500$  in our figures) where the EOF analysis (Fig.9b,e, black curves) revealed a measurable contribution of the beach rotation to the shoreline variability. The best practice is to calibrate the cross-shore model at an alongshore position where the control of longshore processes on shoreline changes is minimized, for instance at  $s$  in the range 1000-2000 m at Narrabeen (Fig. 9b, Fig. 10d,e). This would reduce the risk that the cross-shore model free parameters capture part of the shoreline response to alongshore processes. Future applications of LX-Shore to Narrabeen should explore more precisely the effect of the alongshore location used to calibrate the cross-shore model.

Breaking wave conditions are critical to sediment transport and resulting shoreline change. Simulating the wave field with SWAN (Booij et al., 1999) was required here to reproduce the wave shadowing from the headland and wave energy focusing patterns through wave refraction across the offshore reef. This is not possible with the direct formula of Larson et al. (2010) that both assumes shore-parallel iso-contours (no focusing) and causes alongshore discontinuities in breaking wave energy at the passage from shadowed to non-shadowed regions and vice versa. SWAN includes a module to simulate the wave diffraction, which can occur near the headlands (Daly et al., 2014) and results in wave energy redistribution toward sheltered areas. However, enabling the SWAN diffraction module in our simulations (not shown) resulted in the development of numerical artefacts in simulated wave fields. It also did not affect the wave conditions along the sheltered southern end of the beach for offshore waves coming from the south whereas it should be the case for such conditions. For these reasons, this SWAN module was not used and no diffraction effects were taken into account

in the results presented here. The non-inclusion of the wave diffraction might explain why the overall model performance is degraded at the sheltered southern end of the beach (Fig. 8e, 9b). However, the lack of nearshore wave data in this zone prevents from verifying this speculative hypothesis. It should also be pointed out that wave statistics ( $H_s$ ,  $T_p$ ,  $D_p$ ) were used as offshore wave boundary conditions, although the wave climate off Narrabeen is typically mixed, consisting of locally generated north-easterly waves and swell waves coming predominantly from the SE. Using nested SWAN grids, with the largest grid forced by directional spectra would likely further improve model results, as evidenced by the substantial model improvement by just adding wind effects. Additional simulations (not shown) also indicate that increasing directional spreading, which can reflect an increasingly bimodal wave climate, result in an increasingly curved shoreline planform, i.e. closer to observation at Narrabeen. Therefore, using directional spectra of offshore wave conditions could lead to improved shoreline modelling hindcasts.

The analysis of the spin-up simulations (Fig. 3) revealed that the model spin-up is essentially caused by the alongshore processes (not shown). The model spin-up in the simulation where cross-shore processes are switched off (i.e. longshore only; Fig. 10d,e,k,l) is characterized by a progressive planview shoreline readjustment with erosion along the southern end of the beach and accretion north of the alongshore location of transect PF6. The readjustment rate tends to decrease as the planview shoreline approaches an apparent equilibrium shape. Interestingly, the timescales involved for this alongshore-driven readjustment is relatively long in comparison to the timescales on which the alongshore-driven beach rotation acts. The reason is that these modes of shoreline change are driven by different mechanisms. The beach rotation is stirred by the succession of persistent shifts in the incident wave direction occurring on the

timescales of month to year in the period investigated here. In contrast, the planview shoreline readjustment might results from a disequilibrium on the timescales of several years between the initial planview shoreline and the incident wave conditions along the beach. Indeed, some approximations made for the SWAN wave propagation (e.g. constant directional spreading, binary values for bottom friction coefficient, homogeneous wind) may have led to breaking wave conditions and longshore sediment transport gradients slightly different to those observed at Narrabeen.

Despite the limitations listed above, LX-Shore results show very good agreement with field data. LX-Shore is able to capture even subtle patterns of the dominant spatial modes of shoreline variability. It is important to note that calibration of LX-Shore, which is a one-line model, relies on only four free parameters for the entire embayment. This contrasts with other existing shoreline change models coupling cross-shore and longshore processes (Vitousek et al., 2017; Antolínez et al., 2019), which rely on a specific calibration for every cross-shore transect along the coast. These models therefore require multiple calibration experiments, resulting in a number of free parameters of, at least, an order of magnitude larger than that for LX-Shore. This favours better fitting with field data, but can become a drawback when used for shoreline prediction or at sites with limited shoreline observations. LX-Shore model therefore appears as a relevant and complementary tool to further improve our understanding and predictive ability of shoreline change along real coasts with geological features and exposed to complex wave climates. With both model accuracy and computational power increasing, it is now feasible to simulate multidecadal shoreline change in complex coastal settings. At these timescales sea level rise contribution becomes significant (Le Cozannet et al., 2016) although largely uncertain (Le Cozannet et al., 2019). New developments are being

carried out in LX-Shore to account for the effect of sea level change on shoreline variability (Robinet et al., in revision). This includes the possibility of varying the mean sea level throughout the simulation, which drives slow shoreline retreat based on the Bruun rule (Bruun, 1962) and potentially affects the transformation of onshore-propagating waves across non-erodible offshore bathymetry, and, in turn, breaking wave conditions and sediment transport along the coast. Preliminary tests of shoreline change modelling with LX-Shore involving variations in prevailing wave conditions have been done in the frame of Shorecast (Montaño et al., 2019). Such modelling work may provide new insight into embayed beach behaviour in a changing climate.

## **6 Conclusions**

The hybrid shoreline change model LX-Shore was applied to Narrabeen beach, SE Australia, a high-energy 3.6-km long embayed beach. After calibration on a 4-year time series of shoreline change including a large number of rapid erosion events, multi-month recovery periods and clockwise and counter-clockwise rotation events, the model shows very good agreement with observed shoreline behaviour. Model results show that longshore processes primarily contribute to the second (rotation) and third modes of shoreline variability, while cross-shore processes control the first migration mode. The study showed that the inherent geology strongly modulates spatial variability in the three primary modes of shoreline change. The offshore central rocky outcrop is found to limit the rotation signal at Narrabeen beach. In contrast, the submerged rocky platform prominent extensions from the headlands boost the shoreline rotation mode and increases the alongshore variability of the cross-shore migration mode owing to increased alongshore variability in wave exposure. Accounting for accurate wave transformation in shoreline change modelling appears important to accurately account

for detailed shoreline variability at sites where complex local geology in the nearshore is present. It is anticipated that such a modelling approach may help improve our understanding of shoreline change in a changing climate, even along complex stretches of coast with large geological influence.

## **7 Acknowledgments**

The present work was funded by BRGM and Agence Nationale de la Recherche (ANR) through grants InterCarnot ANR-14&15-BRGM and ANR-147-CE01-0014 (SONO project). The authors are grateful to the WRL team which welcomed Arthur Robinet for a 3-month stay, and to Mike Kinsela from the NSW Office of Environment and Heritage (NSW OEH) for providing the bathymetric contour dataset of Sydney coastal waters. Sydney wave data were kindly provided by the Manly Hydraulics Laboratory on behalf of the NSW OEH. Detailed bathymetric data used in this study were collected by the NSW OEH through the Coastal Processes and Research Node. NOAA and MCIA are also acknowledged for providing wind data, and computations facilities, respectively. Farid Smai from BRGM is thanked for providing support to perform the EOF analyses. Declarations of interest: none.

## **8 References**

Antolínez, J.A.A., Méndez, F.J., Anderson, D., Ruggiero, P., Kaminsky, G.M., 2019. Predicting climate driven coastlines with a simple and efficient multi-scale model, *Journal of Geophysical Research: Earth Surface*, 124, doi: 10.1029/2018JF004790.

Ashton, A.D., Murray, A.B., 2006. High-angle wave instability and emergent shoreline shapes: 1. Modeling of sand waves, flying spits, and capes, *Journal of Geophysical Research*, 111, F04011, doi: 10.1029/2005JF000422.

683 Athanasiou, P., van Dongeren, A., Giardino, A., Vousdoukas, M., Gaytan-Aguilar, S.,  
 684 Ranasinghe, R., 2019. Global distribution of nearshore slopes with implications for  
 685 coastal retreat, *Earth System Science Data*, 11, 1515–1529, doi: 10.5194/essd-11-1515-2019.

686 Bertsimas, D., Tsitsiklis, J., 1993. Simulated annealing, *Statistical Science*, 8, 10–15.

687 Blossier, B., Bryan, K.R., Daly, C. J., Winter, C., 2017. Shore and bar cross-shore migration,  
 688 rotation, and breathing processes at an embayed beach, *Journal of Geophysical Research:*  
 689 *Earth Surface*, 122, 1745–1770, doi: 10.1002/2017JF004227.

690 Booij, N., Ris, R.C., Holthuijsen, L.H., 1999. A third-generation wave model for coastal regions:  
 691 1. Model description and validation, *Journal of Geophysical Research: Oceans*, 104,  
 692 7649–7666, doi: 10.1029/98JC02622.

693 Bouvier, C., Balouin, Y., Castelle, B., 2017. Video monitoring of sandbar-shoreline response to  
 694 an offshore submerged structure at a microtidal beach, *Geomorphology*, 295, 297–305,  
 695 doi: 10.1016/j.geomorph.2017.07.017.

696 Bouvier, C., Castelle, B., Balouin, Y., 2019. Modeling the Impact of the Implementation of a  
 697 Submerged Structure on Surf Zone Sandbar Dynamics, *Journal of Marine Science and*  
 698 *Engineering*, 7 (4), 117, doi: 10.3390/jmse7040117.

699 Bracs, M.A., Turner, I.L., Splinter, K.D., Short, A.D., Lane, C., Davidson, M.A., Goodwin, I.D.,  
 700 Pritchard, T., Cameron, D., 2016. Evaluation of Opportunistic Shoreline Monitoring  
 701 Capability Utilizing Existing “Surfcam” Infrastructure, *Journal of Coastal Research*, 319,  
 702 542–554, doi: 10.2112/JCOASTRES-D-14-00090.1.

703 Bruun, P., 1962. Sea-level rise as a cause of shore erosion, *Journal of the Waterways and*  
 704 *Harbors division*, 88 (1), 117–132.



705 Castelle, B., Coco, G., 2012. The morphodynamics of rip channels on embayed beaches,  
 706 Continental Shelf Research, 43, 10–23, doi: 10.1016/j.csr.2012.04.010.

707 Castelle, B., Coco, G., 2013. Surf zone flushing on embayed beaches, Geophysical Research  
 708 Letters, 40, doi: 10.1002/grl.50485.

709 Castelle, B., Marieu, V., Bujan, S., Ferreira, S., Parisot, J.-P., Capo, S., Sénéchal, N., Chouzenoux,  
 710 T., 2014. Equilibrium shoreline modelling of a high-energy mesomacrotidal multiple-  
 711 barred beach, Marine Geology, 347, 85–94. doi: 10.1016/j.margeo.2013.11.003.

712 Daly, C.J., Bryan, K.R., Winter, C., 2014. Wave energy distribution and morphological  
 713 development in and around the shadow zone of an embayed beach, Coastal  
 714 Engineering, 93, 40–54, doi: 10.1016/j.coastaleng.2014.08.003.

715 Daly, C.J., Winter, C., Bryan, K.R., 2015. On the morphological development of embayed  
 716 beaches, Geomorphology, 248, 252–263, doi: 10.1016/j.geomorph.2015.07.040.

717 Davidson, M.A., Splinter, K.D., Turner, I.L., 2013. A simple equilibrium model for predicting  
 718 shoreline change, Coastal Engineering, 73, 191–202, doi: 10.1016/j.coastaleng.2012.11.002.

719 Dodet, G., Castelle, B., Masselink, G., Scott, T., Davidson, M., Floc’h, F., Jackson, D.W.T.,  
 720 Suanez, S., 2019. Beach recovery from extreme storm activity during the 2013/14 winter  
 721 along the Atlantic coast of Europe, Earth Surface Processes and Landforms, 44 (1), 393–  
 722 401, doi: 10.1002/esp.4500.

723 Durrant, T., Greenslade, D., Hemer, M., Trenham, C., 2014. A global wave hindcast focussed  
 724 on the Central and South Pacific, CAWCR Technical Report No. 70,  
 725 [www.cawcr.gov.au/technical-reports/CTR\\_070.pdf](http://www.cawcr.gov.au/technical-reports/CTR_070.pdf).

726 Fellowes, T.E., Vila-Concejo, A., Gallop, S.L., 2019. Morphometric classification of swell-  
 727 dominated embayed beaches, *Marine Geology*, 411, 78–87,  
 728 doi: 10.1016/j.margeo.2019.02.004.

729 Hallermeier, R., 1981. A profile zonation for seasonal sand beaches from wave climate. *Coastal*  
 730 *Engineering*, 4 (3), 253–277. doi: 10.1016/0378-3839(80)90022-8.

731 Hanson H., 1989. A generalized shoreline change numerical model, *Journal of Coastal*  
 732 *Research*, 5, 1–27.

733 Hanson, H., Brampton, A., Capobianco, M., Dette, H.H., Hamm, L., Laustrop, C., Lechuga, A.,  
 734 Spanhoff, R., 2002. Beach nourishment projects, practices, and objectives - a European  
 735 overview, *Coastal Engineering*, 47, 81–111, doi: 10.1016/S0378-3839(02)00122-9.

736 Harley, M.D., Turner, I.L., 2008. A simple data transformation technique for pre-processing  
 737 survey data at embayed beaches, *Coastal Engineering*, 55 (1), 63–68.  
 738 doi: 10.1016/j.coastaleng.2007.07.001.

739 Harley, M.D., Turner, I.L., Short, A.D., Ranasinghe, R., 2010. Interannual variability and  
 740 controls of the Sydney wave climate, *International Journal of Climatology*, 30, 1322–1335,  
 741 doi: 10.1002/joc.1962

742 Harley, M.D., Turner, I.L., Short, A.D., Ranasinghe, R., 2011a. A reevaluation of coastal  
 743 embayment rotation: The dominance of cross-shore versus alongshore sediment  
 744 transport processes, Collaroy-Narrabeen Beach, southeast Australia, *Journal of*  
 745 *Geophysical Research*, 116, F04033, doi: 10.1029/2011JF001989.

746 Harley, M.D., Turner, I.L., Short, A.D., Ranasinghe, R., 2011b. Assessment and integration of  
 747 conventional, RTK-GPS and image-derived beach survey methods for daily to decadal

748 coastal monitoring, Coastal Engineering, 58 (2), 194–205,  
 749 doi: 10.1016/j.coastaleng.2010.09.006

750 Harley, M.D., Andriolo, U., Armaroli, C., Ciavola, P., 2013. Shoreline rotation and response to  
 751 nourishment of a gravel embayed beach using a low-cost video monitoring technique:  
 752 San Michele-Sassi Neri, central Italy, Journal of Coastal Conservation, 18, 551–565,  
 753 doi: 10.1007/s11852-013-0292-x.

754 Harley, M.D., Turner, I.J., Short, A.D., 2015. New insights into embayed beach rotation: The  
 755 importance of wave exposure and cross-shore processes, Journal of Geophysical  
 756 Research: Earth Surface, 120, 1470–1484, doi: 10.1002/2014JF003390.

757 Hurst, M.D., Barkwith, A., Ellis, M.A., Thomas, C.W., Murray, A.B., 2015. Exploring the  
 758 sensitivities of crenulate bay shorelines to wave climates using a new vector-based one-  
 759 line model, Journal of Geophysical Research: Earth Surface, 120, 2586–2608,  
 760 doi: 10.1002/2015JF003704.

761 Jackson, D.W.T., Cooper, J.A.G., Rio, L.D., 2005. Geological control of beach morphodynamic  
 762 state, Marine Geology, 216,297–314, doi: 10.1016/j.margeo.2005.02.021.

763 Kaergaard, K., Fredsoe, J., 2013. A numerical shoreline model for shorelines with large  
 764 curvature, Coastal Engineering, 74, 19–32. doi: 10.1016/j.coastaleng.2012.11.011.

765 Kamphuis, J.W., 1991. Alongshore sediment transport rate, Journal of Waterway, Port, Coastal,  
 766 and Ocean Engineering, 117 (6), 624–641, doi: 10.1061/(ASCE)0733-950X(1991)117:6(624).

767 Klein, A.H.F., Benedet, L., Schumacher, D.H., 2002. Short-term beach rotation processes in  
 768 distinct headland bay beach systems, Journal of Coastal Research, 18 (3), 442–458.

769 Komen, G.J., Hasselmann, S. , Hasselmann, K., 1984. On the existence of a fully developed  
770 wind-sea spectrum, *Journal of Physical Oceanography*, 14, 1271–1285, doi: 10.1175/1520-  
771 0485(1984)014<1271:OTEOAF>2.0.CO;2.

772 Larson, M., Hoan, L.X., Hanson, H., 2010. Direct formula to compute wave height and angle  
773 at incipient breaking, *Journal of Waterway Port Coastal and Ocean Engineering*, 136 (2),  
774 119–122, doi: /10.1061/(ASCE)WW.1943-5460.0000030.

775 Le Cozannet, G., Oliveros, C., Castelle, B., Garcin, M., Idier, D., Pedreros, R., Rohmer, J., 2016.  
776 Uncertainties in Sandy Shorelines Evolution Under the Bruun Rule Assumption,  
777 *Frontiers in Marine Science*, 3, 49, doi: 10.3389/fmars.2016.00049.

778 Le Cozannet, G., Bulteau, T., Castelle, B., Ranasinghe, R., Woppelmann, G., Rohmer, J., Bernon,  
779 N., Idier, D., Louisor, J., Salas-y-Mélia, D., 2019. Quantify Uncertainties of Sandy  
780 Shoreline Change Projections as Sea Level Rises, *Scientific Reports*, 9, 42,  
781 doi: 10.1038/s41598-018-37017-4.

782 Limber, P.W., Adams, P.N., Murray, B., 2017. Modeling large-scale shoreline change caused  
783 by complex bathymetry in low-angle wave climates, *Marine Geology*, 383, 55–64,  
784 doi: 10.1016/j.margeo.2016.11.006.

785 Loureiro, C., Ferreira, O., Cooper, J.A.G., 2012. Extreme erosion on high-energy embayed  
786 beaches: influence of megarips and storm grouping, *Geomorphology*, 139–140, 155–171,  
787 doi: 10.1016/j.geomorph.2011.10.013.

788 Loureiro, C., Ferreira, O., Cooper, J.A.G., 2013. Geologically constrained morphological  
789 variability and boundary effects on embayed beaches, *Marine Geology*, 329–331, 1–15,  
790 doi: 10.1016/j.margeo.2012.09.010.

791 Madsen, O. S., Poon, Y.-K., Graber, H. C., 1988. Spectral wave attenuation by bottom friction:  
 792 Theory, Proceedings of the 21st Coastal Engineering Conference, ASCE.

793 Masselink, G., Pattiaratchi, C.B., 2001. Seasonal changes in beach morphology along the  
 794 sheltered coastline of Perth, Western Australia, *Marine Geology*, 172 (3–4), 243–263,  
 795 doi: 10.1016/S0025-3227(00)00128-6.

796 McCarroll, J., Masselink, G., Valiente, N. G., Scott, T., King, E., 2018. Wave and tidal controls  
 797 on headland bypassing and embayment circulation, *Journal of Marine Science and*  
 798 *Engineering*, 6 (3), 94, doi: doi.org/10.3390/jmse6030094.

799 Miller, J.K., Dean, R.G., 2007. Shoreline variability via empirical orthogonal function analysis:  
 800 Part I. Temporal and spatial characteristics, *Coastal Engineering*, 54 (2), 111–131,  
 801 doi: 10.1016/j.coastaleng.2006.08.013.

802 Montaña, J., Coco, G., Antolínez, J.A., Beuzen, T., Bryan, K., Cagical, L., Castelle, B., Davidson,  
 803 M., Goldstein, E., Ibaceta Vega, R., Ludka, B., Massoud Ansari, S., Mendez, F., Murray,  
 804 B., Plant, N., Robinet, A., Rueda, A., Senechal, N., Simmons, J., Splinter, K.D., Stephens,  
 805 S., Towned, I., Vitousek, S., Vos, K., 2019. Shorecasts: a blind-test of shoreline models,  
 806 *Proceedings of the Coastal Sediments 2019*, 627–631, doi: 10.1142/9789811204487\_0055.

807 Morris, B.D., Turner, I.L., 2010. Morphodynamics of intermittently open-closed coastal lagoon  
 808 entrances: New insights and a conceptual model, *Marine Geology*, 271 (1–2), 55–66,  
 809 doi: 10.1016/j.margeo.2010.01.009.

810 Ojeda, E., Guillen, J., 2008. Shoreline dynamics and beach rotation of artificial embayed  
 811 beaches, *Marine Geology*, 253, 51–62, doi: 10.1016/j.margeo.2008.03.010.

812 Ortiz, A.C., Ashton, A.D., 2016. Exploring shoreface dynamics and a mechanistic explanation  
 813 for a morphodynamic depth of closure, *Journal of Geophysical Research: Earth Surface*,  
 814 121, 442–464, doi: 10.1002/2015JF003699.

815 Ranasinghe R., McLoughlin R., Short A., Symonds G., 2004. The Southern Oscillation Index,  
 816 wave climate, and beach rotation, *Marine Geology*, 204, 273–287, doi: 10.1016/S0025-  
 817 3227(04)00002-7.

818 Ratliff, K.M., Murray, A.B., 2014. Modes and emergent time scales of embayed beach  
 819 dynamics, *Geophysical Research Letters*, 41, 7270–7275, doi: 10.1002/2014GL061680.

820 Robinet, A., Idier, D., Castelle, B., Marieu, V., 2018. A reduced-complexity shoreline change  
 821 model combining longshore and cross-shore processes: The LX-Shore model,  
 822 *Environmental Modelling & Software*, 109, 1–16, doi: 10.1016/j.envsoft.2018.08.010.

823 Robinet, A., Castelle, B., Idier, D., D’Anna, M., Le Cozannet, G., in revision, Simulating the  
 824 Impact of Sea-Level Rise and Offshore Bathymetry on Embayment Shoreline Changes,  
 825 In: Malvárez, G. and Navas, F. (eds.), *Proceedings from the International Coastal*  
 826 *Symposium (ICS) 2020 (Seville, Spain)*, *Journal of Coastal Research*, Special Issue No. 95,  
 827 pp. 1–5. Coconut Creek (Florida), ISSN 0749-0208.

828 Short, A.D., Masselink G., 1999. Embayed and structurally controlled beaches, in : Short, A.D.  
 829 (Editor) *Handbook of Beach and Shoreface Morphodynamics*, John Wiley & Sons,  
 830 Chichester, 230–250.

831 Short, A.D., Trembanis, A.C., 2004. Decadal scale patterns in beach oscillation and rotation  
 832 Narrabeen beach, Australia—Time series, PCA and wavelet analysis, *Journal of Coastal*  
 833 *Research*, 20 (2), 523–532.

834 Splinter, K.D., Turner, I.L., Davidson, M.A., 2013. How much data is enough? The importance  
 835 of morphological sampling interval and duration for calibration of empirical shoreline  
 836 models, *Coastal Engineering*, 77, 14–27, doi: 10.1016/j.coastaleng.2013.02.009.

837 Splinter, K.D., Turner, I.L., Davidson, M.A., Barnard, P., Castelle, B., Oltman-Shay, J., 2014. A  
 838 generalized equilibrium model for predicting daily to interannual shoreline response,  
 839 *Journal of Geophysical Research: Earth Surface*, 119 (9), 1936–1958,  
 840 doi: 10.1002/2014JF003106.

841 Splinter, K.D., Turner, I.L., Reinhardt, M., Ruessink, B.G., 2017. Rapid adjustment of shoreline  
 842 behaviour to changing seasonality of storms: observations and modelling at an open-  
 843 coast beach, *Earth Surface Processes and Landforms*, 42, 1886–1194,  
 844 doi: 10.1002/esp.4088.

845 Splinter, K.D., Kearney, E.T., Turner, I.L., 2018. Drivers of alongshore variable dune erosion  
 846 during a storm event: Observations and modelling, *Coastal Engineering*, 131, 31–41, doi:  
 847 10.1016/j.coastaleng.2017.10.011.

848 Thom, B.G., 1983. Transgressive and regressive stratigraphies of coastal sand barriers in  
 849 southeast Australia, *Marine Geology*, 56, 137–158, doi: 10.1016/0025-3227(84)90010-0.

850 Thomas, T., Phillips, M.R., Williams, A.T., 2010. Mesoscale evolution of a headland bay: beach  
 851 rotation process, *Geomorphology*, 123, 129–141, doi: 10.1016/j.geomorph.2010.06.018.

852 Turki, I., Medina, R., Coco, G., Gonzalez, M., 2013. An equilibrium model to predict shoreline  
 853 rotation of pocket beaches, *Marine Geology*, 346, 220–232,  
 854 doi: 10.1016/j.margeo.2013.08.002.

855 Turner, I.L., Harley, M.D., Short, A.D., Simmons, J.A., Bracs, M.A., Phillips, M.S., Splinter,  
 856 K.D., 2016. A multi-decade dataset of monthly beach profile surveys and inshore wave  
 857 forcing at Narrabeen, Australia, *Science Data*, 3 (160024), doi: 10.1038/sdata.2016.24.

858 Valiente, N.G., Masselink, G., Scott, T., Conley, D., McCarroll, J., 2019. Evaluation of the role  
 859 of waves and tides on depth of closure and potential for headland bypassing, *Marine*  
 860 *Geology*, 407, 60–75, doi: 10.1016/j.margeo.2018.10.009.

861 Van de Lageweg, W.I., Bryan, K.R., Coco, G., Ruessink, B.G., 2013. Observations of shoreline–  
 862 sandbar coupling on an embayed beach, *Marine Geology*, 344, 101–114,  
 863 doi: 10.1016/j.margeo.2013.07.018.

864 Vitousek, S., Barnard, P.L., Limber, P., Erikson, L., Cole, B., 2017. A model integrating  
 865 longshore and cross-shore processes for predicting long-term shoreline response to  
 866 climate change, *Journal of Geophysical Research: Earth Surface*, 122 (4), 782–806,  
 867 doi: 10.1002/2016JF004065.

868 Whiteway, T.G., 2009. Australian Bathymetry and Topography Grid, June 2009, *Geoscience*  
 869 *Australia Record* 2009/21, 46pp.

870 Yates, M.L., Guza, R.T., O'Reilly, W.C., 2009. Equilibrium shoreline response: observations and  
 871 modelling, *Journal of Geophysical Research*, 114, doi: 10.1029/2009JC005359.C09014.



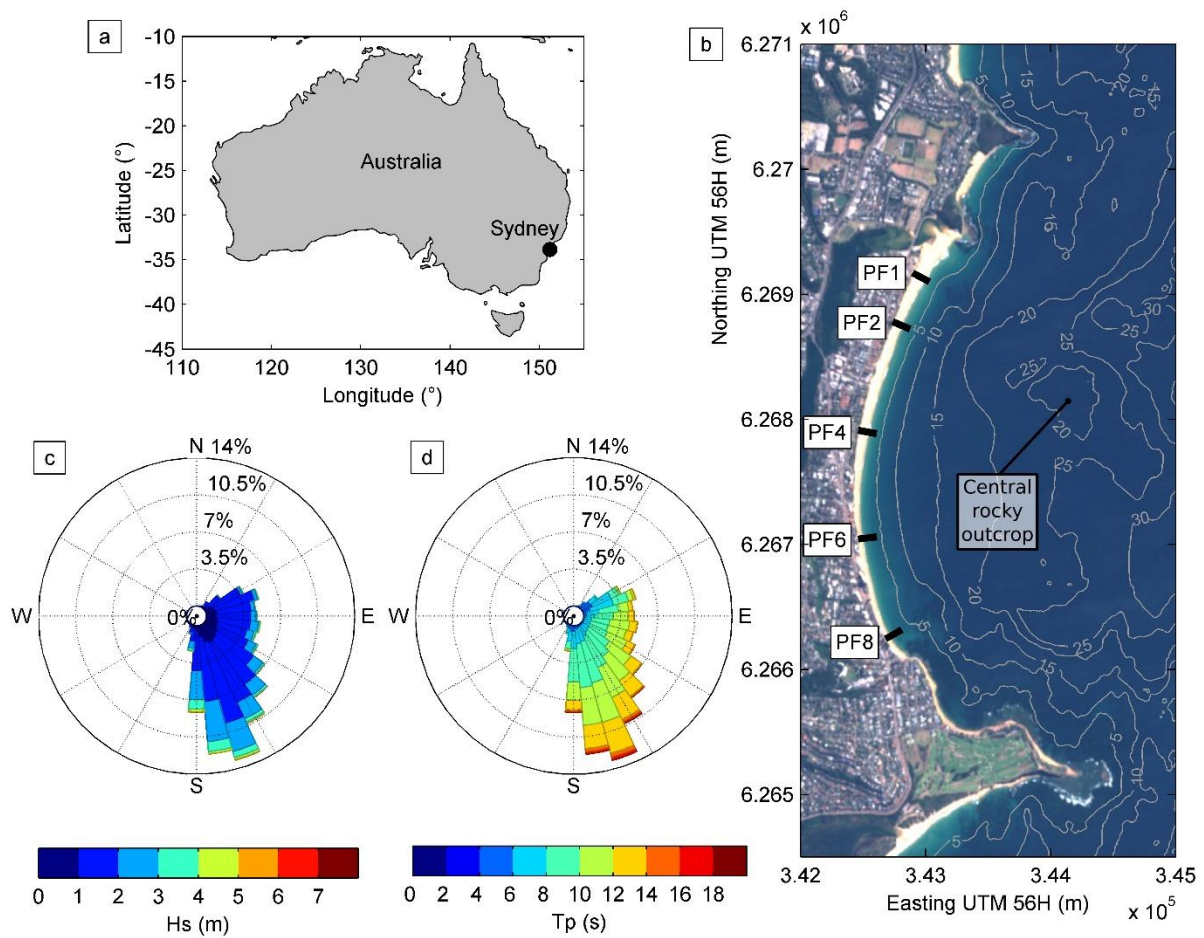


Figure 1 – (a) Location map of (b) Narrabeen beach (Sydney, NSW, Australia) shown by a Sentinel-2 image with bathymetric contours superimposed. The black ticks in (b) indicate the location of five of the historical transects where beach profiles have been acquired since 1976. Wave roses for (c) significant wave height  $H_s$  and (d) peak wave period  $T_p$  measured at Sydney buoy from July 2006 to July 2010 (for the location of the Sydney buoy, see Fig. 4a).

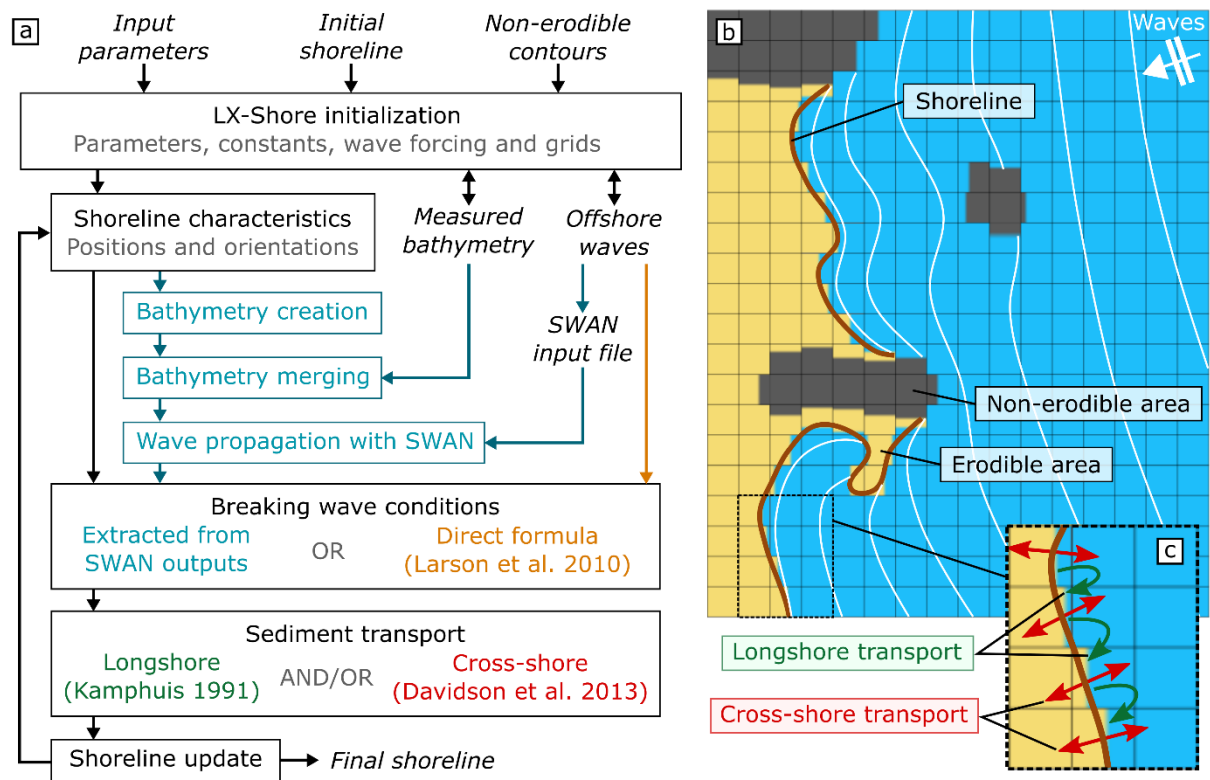


Figure 2 – Overview of LX-Shore. (a) Architecture and functionalities. (b,c) Illustrations of the main physical processes included in the model. For more detail the reader is referred to Robinet et al. (2018).

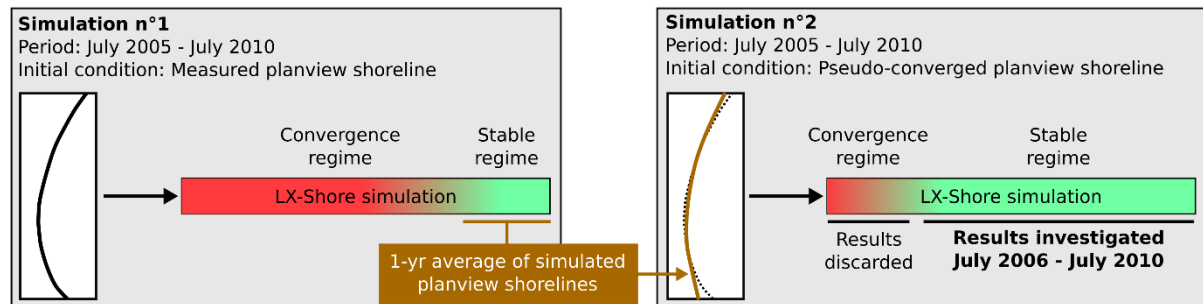


Figure 3 – The two-step simulation workflow used to reduce the impact of model spin-up from the initial measured shoreline.

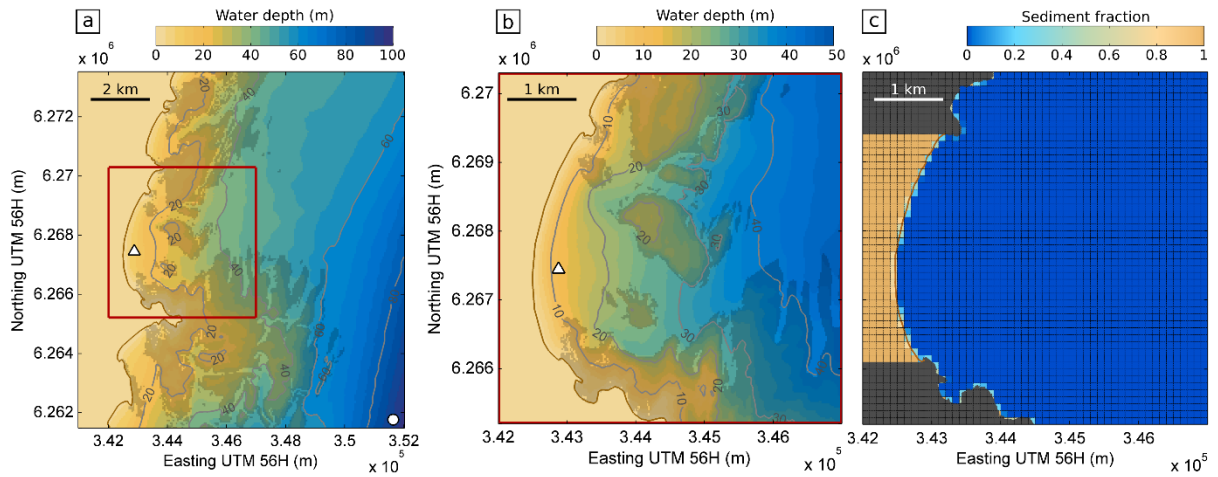


Figure 4 – (a) Coarse and (b) refined nested grid bathymetries used with SWAN. (c) Example of sediment fraction distribution over the morphological grid. The bathymetry shown in (b) is the merged bathymetry produced by LX-Shore on September 20, 2005. The red contour in panel (a) indicates the extent of the refined nested hydrodynamic grid. The white circle in panel (a) locates the Sydney buoy. The white triangle in panels (a,b) locates the inshore buoy location. The shaded areas in panels (a,b) denote the presence of rocky seabed. The dark grey areas in panel (c) indicate non-erodible areas.

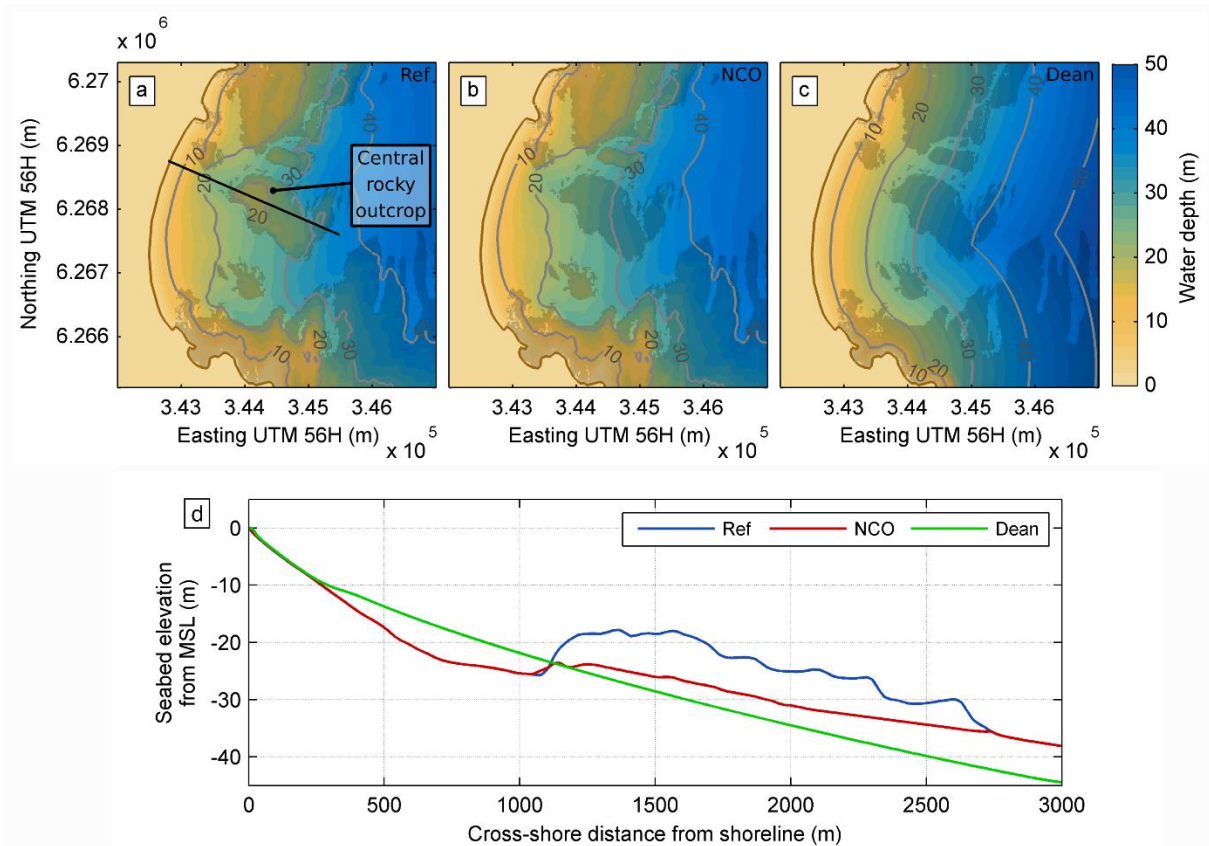


Figure 5 – (a) Merged bathymetry produced by LX-Shore on September 20, 2005 for the reference simulation, (b) without the central rocky outcrop and (c) further idealizing the bathymetry using a Dean profile along the entire embayment. (d) Seabed elevation extracted from the bathymetries shown in panels (a,b,c) along the PF2 transect extending up to 3 km offshore (black line in panel a). In panels (a,b,c) the shaded areas indicate the location of non-erodible rocky seabed.

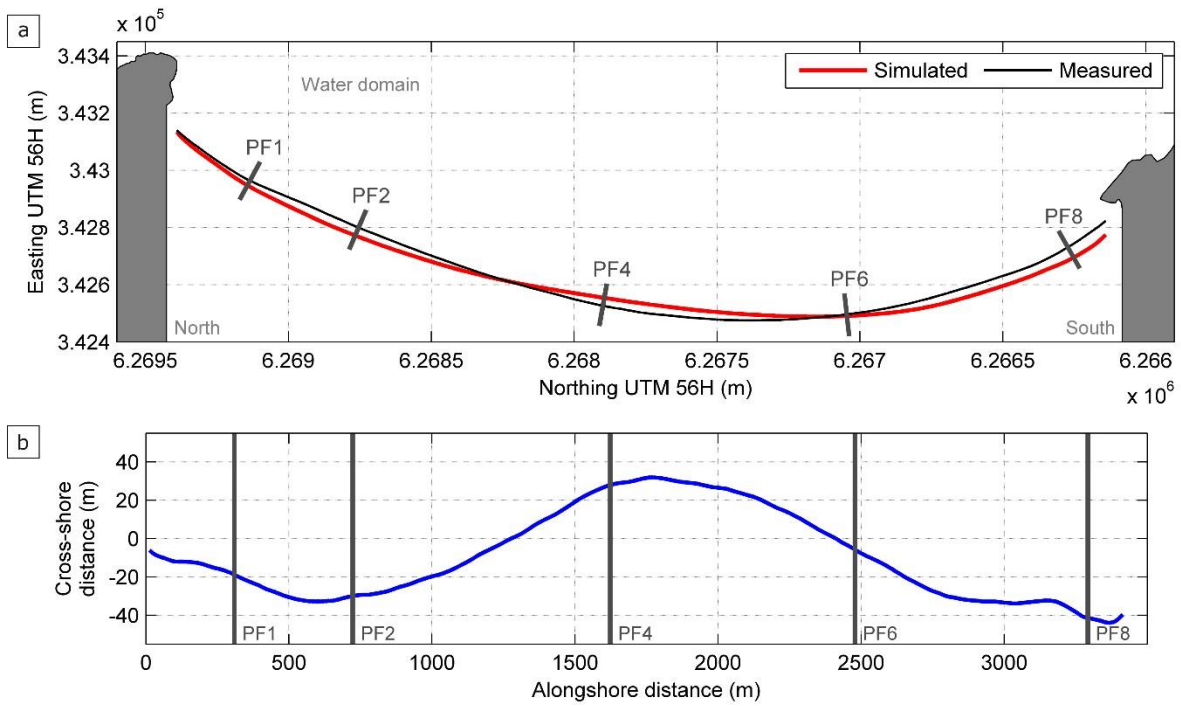


Figure 6 – (a) Time average (July 2006 – July 2010) of measured (black) and modelled (red and thick) planview shorelines. (b) Cross-shore distance (blue) between the planview shorelines shown in panel (a).

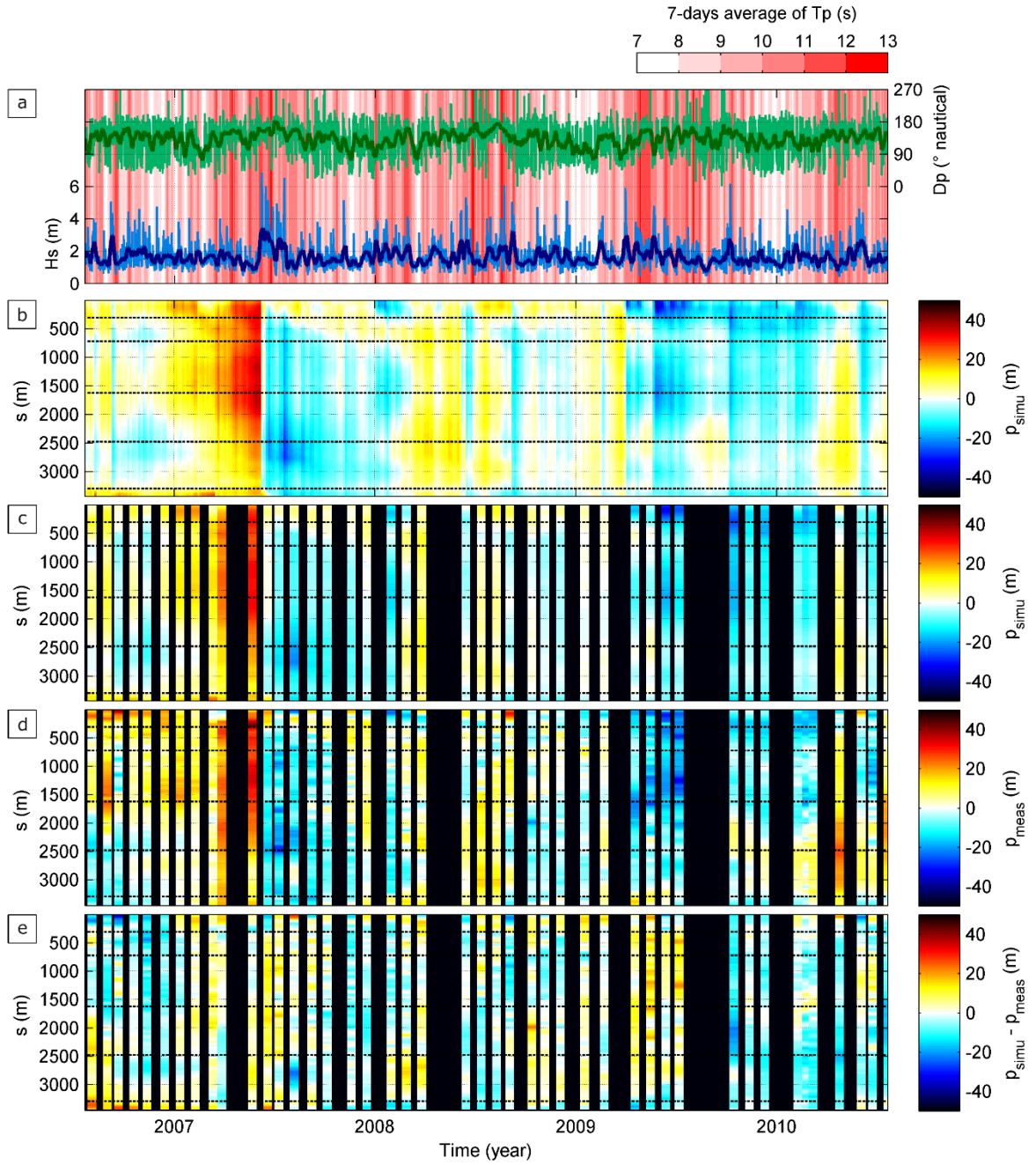
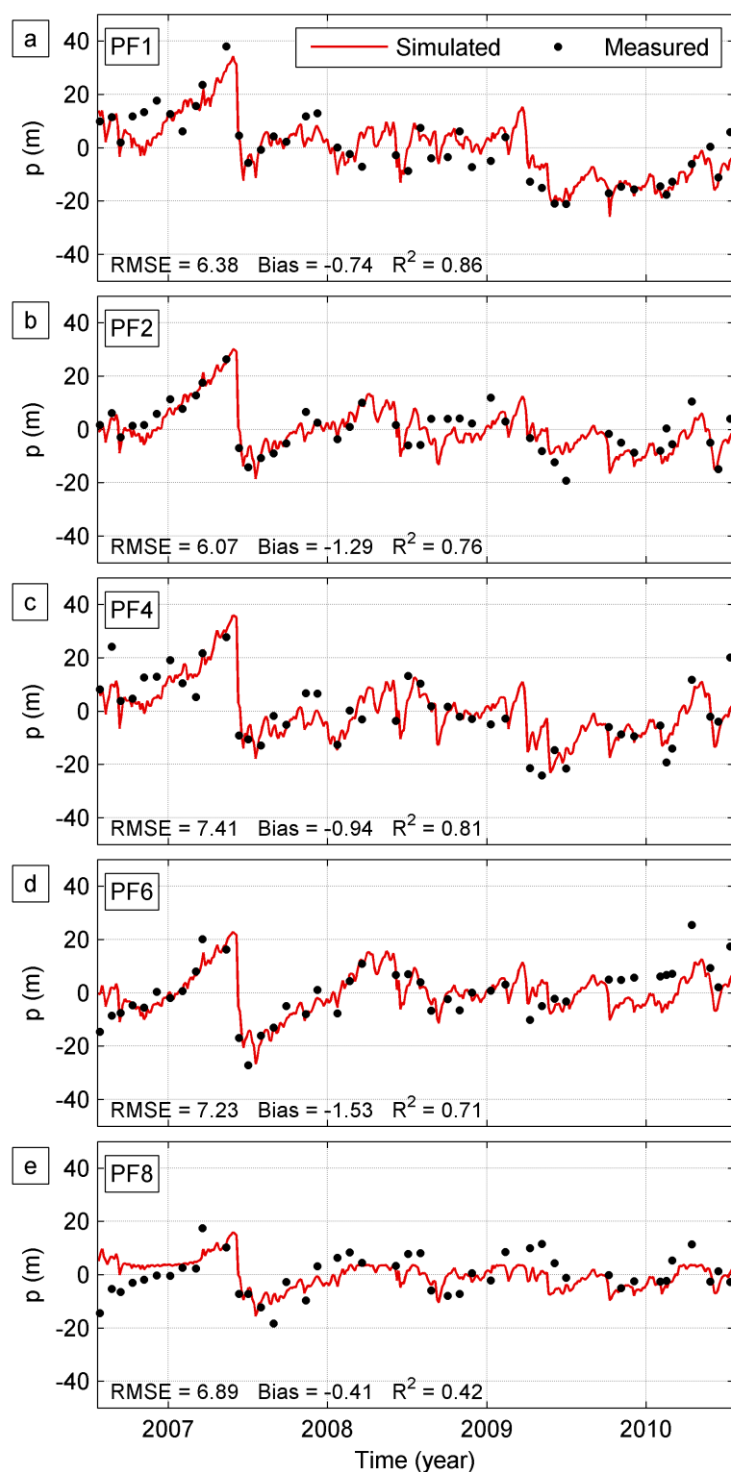


Figure 7 – (a) Times series of offshore wave conditions with thin and thick lines indicating respectively hourly and 7-day-averaged wave conditions for  $H_s$  (blue) and  $D_p$  (green) and the red background colour indicating the 7-day average of  $T_p$ . (b,c,d) Shoreline deviation from the mean  $p(s,t)$  at Narrabeen beach : (b) modelled with shoreline position at each model time step (3 hours); (c) modelled only at the time steps concurrent with measurements; (d) obtained from measurements. (e) Difference between the space-time diagrams shown in panels (c,d). In panels (b,c,d,e) the horizontal dashed lines show the location of the cross-shore transects PF1-8 shown in Fig. 1 and Fig. 6. In panels (b,c,d,e) the  $s$  value of the  $y$ -axis indicates the alongshore distance from the north.

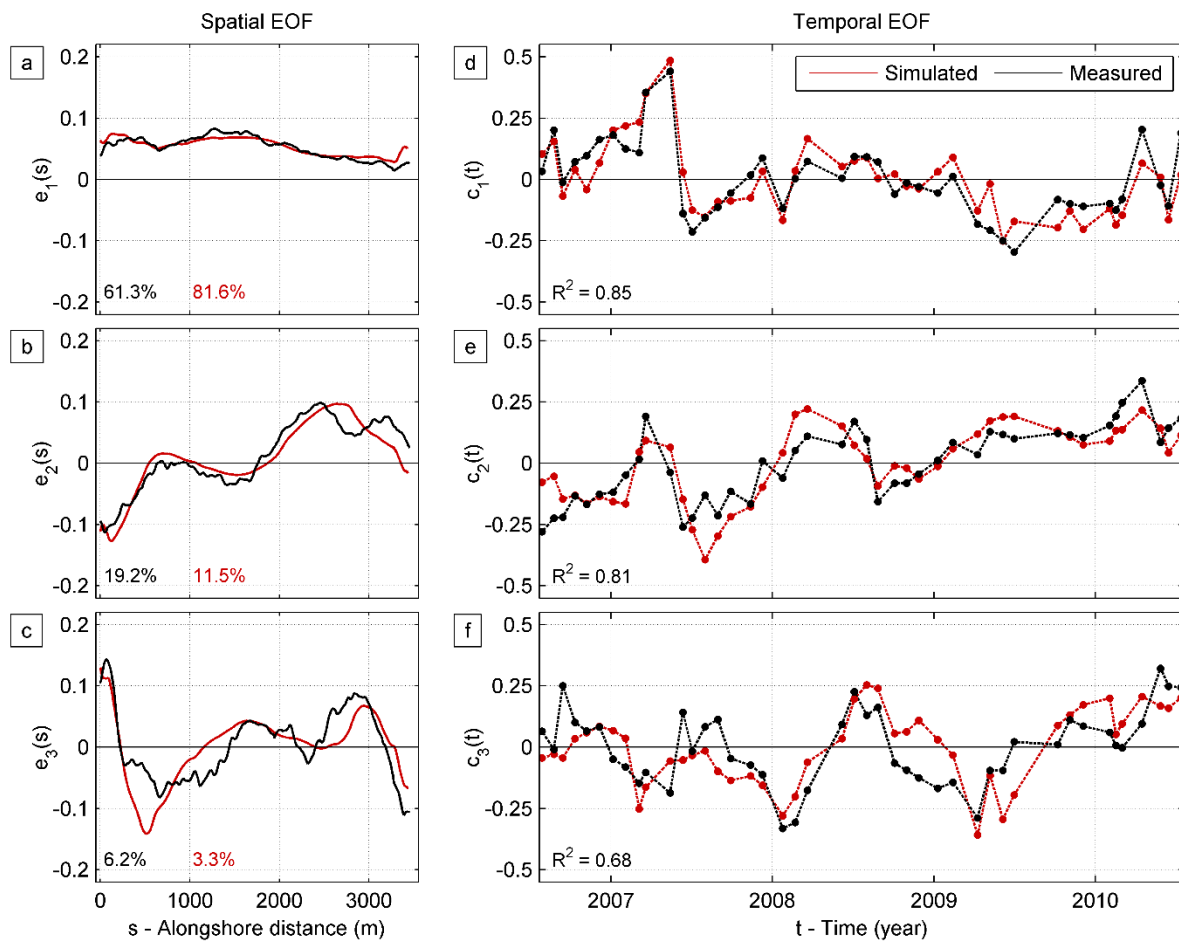




914

915 *Figure 8 – Time series of measured (black dots) and simulated (continuous red line) cross-shore shoreline deviation*  
 916 *from the mean  $p(t)$  at profiles PF1 (a), PF2 (b), PF4 (c), PF6 (d), and PF8 (e). For each profile, root-mean-square*  
 917 *error, bias and R-squared values are indicated. See Fig. 1 and Fig. 6 for the transect location.*

918



919

920 Figure 9 – EOF analyses of the  $p(s,t)$  matrices: (a,d) first, (b,e) second and (c,f) third spatial and temporal EOFs.

921



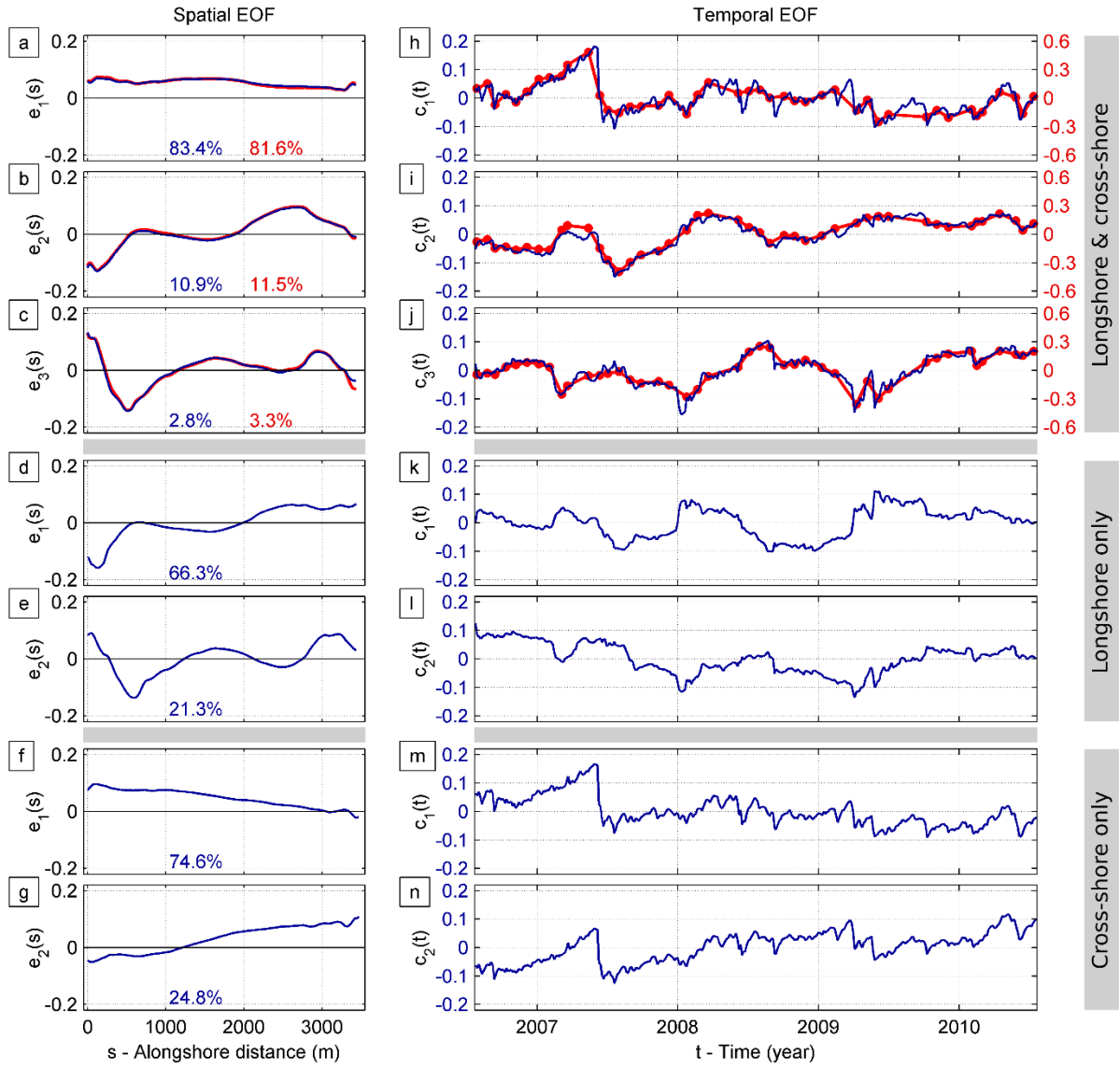


Figure 10 – EOF analyses of the  $p(s,t)$  matrices with the dominant spatial and temporal modes of the simulations (a,b,c,h,i,j) combining cross-shore and longshore processes; (d,e,k,l) accounting for longshore processes only and (f,g,m,n) accounting for cross-shore processes only. Blue (all panels) and red (panels a,b,c,h,i,j) colours are for EOF analyses computed using simulation outputs at each model time step and only those concurrent with measurements, respectively.

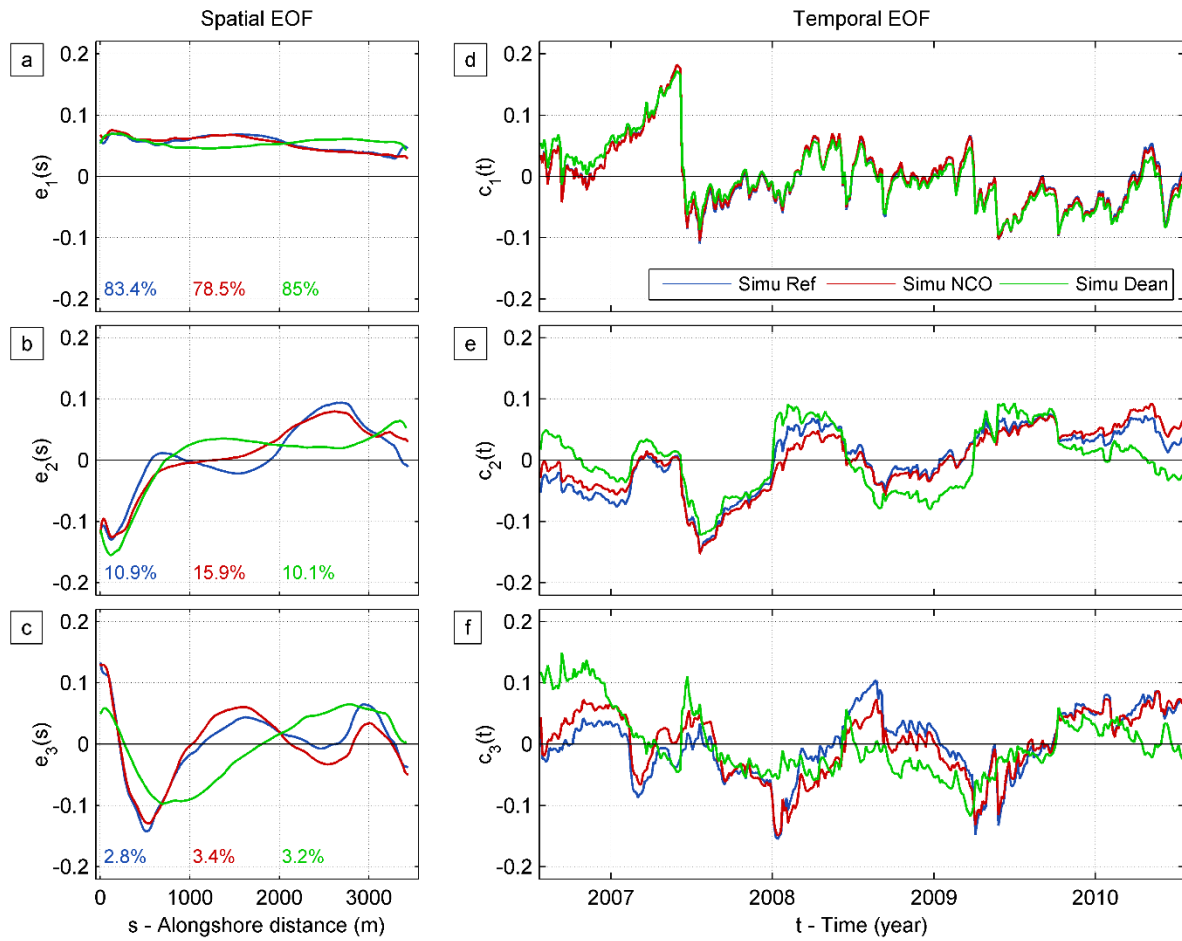


Figure 11 – EOF analyses of the  $p(s,t)$  matrices with the dominant (a,b,c) spatial and (e,f,g) temporal modes of shoreline variability using model outputs at each time step. Reference simulation ('Simu Ref', in blue) without the central rocky outcrop ('Simu NCO', in red) and further removing the submerged rocky platforms extensions from the headlands ('Simu Dean', in green) are superimposed. See Fig. 5 for the corresponding nearshore bathymetries.

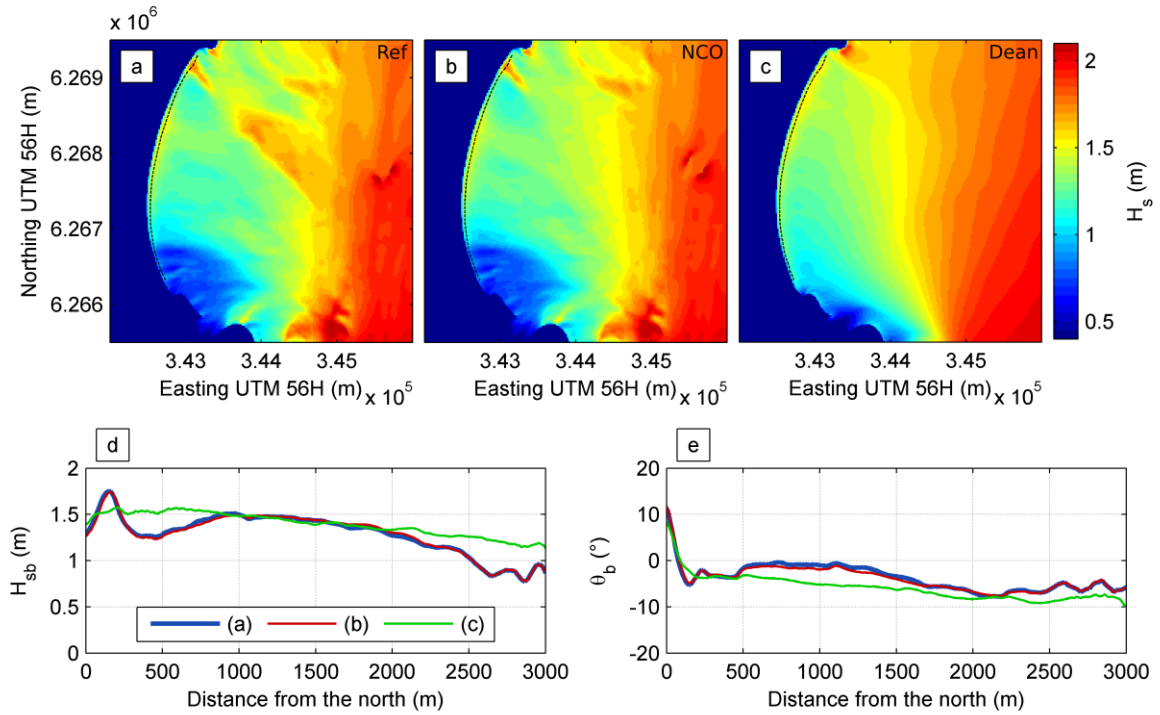


Figure 12 – (a,b,c)  $H_s$  field simulated with SWAN for above average offshore wave conditions from SE ( $H_s = 2.3$  m,  $T_p = 11.1$  s,  $D_p = 164^\circ$  TN) using the bathymetry shown in panels (a,b,c) of Fig. 5, respectively. (d,e) Alongshore distribution of  $H_s$  and incidence angle ( $\theta$ ) extracted at breaking corresponding to these simulated wave fields. Negative values for  $\theta$  represent wave angles oriented southwards with respect to the local coast orientation, and vice versa. The thin dotted lines in panels (a,b,c) indicate the breaking line.

Table 1 – Skill parameters of wave parameters in 10-m depth after SWAN calibration.

	$R$	Bias	RMSE
$H_s$	0.94	0.03 m	0.17 m
$T_m$	0.60	- 0.57 s	1.54 s
$D_m$	0.75	0.71 °	10.13 °